

1 **The assembly of neutrophil inflammasomes during COVID-19 is mediated by type I**  
2 **interferons**

3 **Luz E. Cabrera<sup>1,\*</sup>, Suvi T. Jokiranta<sup>2,3</sup>, Sanna Mäki<sup>1</sup>, Simo Miettinen<sup>1,4</sup>, Ravi Kant<sup>1,4,5</sup>,**  
4 **Lauri Kareinen<sup>1,4</sup>, Tarja Sironen<sup>1,4</sup>, Jukka-Pekka Pietilä<sup>6,7</sup>, Anu Kantele<sup>6,7</sup>, Eliisa**  
5 **Kekäläinen<sup>2,3,10</sup>, Hanna Lindgren<sup>11</sup>, Pirkko Mattila<sup>11</sup>, Anja Kipar<sup>4,8,9</sup>, Olli Vapalahti<sup>1,4,10</sup>**  
6 **and Tomas Strandin<sup>1</sup>**

7

8 <sup>1</sup>Viral Zoonosis Research Unit, Medicum, Department of Virology, University of Helsinki, Helsinki,  
9 Finland.

10 <sup>2</sup>Department of Bacteriology and Immunology, University of Helsinki, Helsinki, Finland.

11 <sup>3</sup>Translational Immunology Research Program, Faculty of Medicine, University of Helsinki, Helsinki,  
12 Finland.

13 <sup>4</sup>Department of Veterinary Biosciences, University of Helsinki, Helsinki, Finland.

14 <sup>5</sup>Department of Tropical Parasitology, Institute of Maritime and Tropical Medicine, Medical University  
15 of Gdansk, 81-519 Gdynia, Poland.

16 <sup>6</sup>Human Microbiome Research Program, Faculty of Medicine, University of Helsinki, Helsinki,  
17 Finland.

18 <sup>7</sup>Meilahti Vaccine Research Center MeVac, Department of Infectious Diseases, Inflammation Center,  
19 Helsinki University Hospital and University of Helsinki, Helsinki, Finland.

20 <sup>8</sup>Laboratory for Animal Model Pathology, Institute of Veterinary Pathology, Vetsuisse Faculty,  
21 University of Zurich, 8057 Zurich, Switzerland.

22 <sup>9</sup>Department of Infection Biology & Microbiomes, Institute of Infection, Veterinary and Ecological  
23 Sciences, University of Liverpool, Liverpool L3 3RF, UK.

24 <sup>10</sup>Division of Virology and Immunology, HUSLAB Clinical Microbiology, HUS Diagnostic Center,  
25 Helsinki University Hospital, Helsinki, Finland.

26 <sup>11</sup>Institute for Molecular Medicine Finland (FIMM), HiLIFE, University of Helsinki, Helsinki, Finland.

27 **NOTE: This preprint reports new research that has not been certified by peer review and should not be used to guide clinical practice.**

28 **Abstract**

29 The severity of COVID-19 is linked to excessive inflammation. Neutrophils represent a critical  
30 arm of the innate immune response and are major mediators of inflammation, but their role in  
31 COVID-19 pathophysiology remains poorly understood. We conducted transcriptomic  
32 profiling of neutrophils obtained from patients with mild and severe COVID-19, as well as  
33 from SARS-CoV-2 infected mice, in comparison to non-infected healthy controls. In addition,  
34 we investigated the inflammasome formation potential in neutrophils from patients and mice  
35 upon SARS-CoV-2 infection. Transcriptomic analysis of polymorphonuclear cells (PMNs),  
36 consisting mainly of mature neutrophils, revealed a striking type I interferon (IFN-I) gene  
37 signature in severe COVID-19 patients, contrasting with mild COVID-19 and healthy controls.  
38 Notably, low-density granulocytes (LDGs) from severe COVID-19 patients exhibited an  
39 immature neutrophil phenotype and lacked this IFN-I signature. Moreover, PMNs from severe  
40 COVID-19 patients showed heightened nigericin-induced caspase1 activation, but reduced  
41 responsiveness to exogenous inflammasome priming. Furthermore, IFN-I emerged as a  
42 priming stimulus for neutrophil inflammasomes, which was confirmed in a COVID-19 mouse  
43 model. These findings underscore the crucial role of neutrophil inflammasomes in driving  
44 inflammation during severe COVID-19. Altogether, these findings open promising avenues for  
45 targeted therapeutic interventions to mitigate the pathological processes associated with the  
46 disease.

47

48 **Keywords:** inflammasome, neutrophils, COVID-19, type I interferon, inflammation, innate  
49 immunity.

## 50 **Introduction**

51

52 Severe COVID-19 is characterized by a dysregulated immune response with an excessive  
53 production of pro-inflammatory cytokines and chemokines. Type I interferons (IFN-I) are  
54 critical antiviral cytokines in the innate immune responses against viral infections, drawing  
55 particular attention amidst the COVID-19 pandemic <sup>1-3</sup>. While the IFN-I response helps to limit  
56 virus replication <sup>3</sup>, its prolonged and uncontrolled activation is detrimental to the overall health  
57 of the patient <sup>4</sup>. As part of the pro-inflammatory response, neutrophils are rapidly recruited to  
58 the site of infection in response to SARS-CoV-2 infection <sup>5,6</sup>. Prominent neutrophil recruitment  
59 in severe COVID-19 is associated with an increased number of immature low-density  
60 granulocytes (LDGs) in the circulation <sup>7-9</sup>. The increased production and subsequent early  
61 release of immature cells from the bone marrow occurs in response to emergency myelopoiesis  
62 <sup>9</sup>. This process is initiated by the body to enable the recruitment of innate immune cells into  
63 the tissues and to replenish the depleted leukocyte pool, in an effort to combat viral infections  
64 including SARS-CoV-2 <sup>10</sup>. However, the premature release of these cells could be associated  
65 with the increased degranulation and formation of neutrophil extracellular traps (NETs)  
66 reported during SARS-CoV-2 infection, to which LDGs have a higher propensity than  
67 polymorphonuclear cells (PMN) <sup>5,6,11</sup>.

68

69 Neutrophils are involved in several aspects of inflammatory processes, including the release of  
70 reactive oxygen species (ROS) and other pro-inflammatory mediators such as Interleukin-6  
71 (IL-6) and IL-8. In addition, recent reports on COVID-19 highlight that neutrophils could be a  
72 major source of inflammasome derived IL-1 $\beta$ , which has been implicated as a substantial  
73 contributor to COVID-19 pneumonia <sup>12</sup>. Inflammasomes are intracellular multiprotein  
74 complexes involved in the inflammatory response. In the presence of a pathogen, antigen

75 recognition by the immune system triggers the assembly of the inflammasome, a step known  
76 as the first signal. This is followed by the recruitment of adaptor molecules that activate NOD-  
77 like receptor (NLR) family members and the binding of the apoptosis-associated speck-like  
78 protein (ASC), finally activating the inflammasome complex <sup>13</sup>. The triggered assembly of this  
79 complex is known as the second signal. Studies have shown that SARS-CoV-2 infection  
80 induces significant inflammasome activation in circulating and lung-infiltrating myeloid cells,  
81 such as monocytes and neutrophils <sup>14-17</sup>. However, while the precise mechanism by which  
82 inflammasomes are activated in monocytes/macrophages is well established, less is known  
83 about molecular mechanisms of inflammasome formation in neutrophils. Thus, this study  
84 investigates the inflammasome formation in neutrophils during COVID-19 in more detail, also  
85 focusing on the different developmental stages of these cells. In addition, a recently established  
86 COVID-19 mouse model served to further explore the role of IFN-I in neutrophil  
87 inflammasome assembly.



## 88 **Materials and methods**

### 89 **Patient population**

90 Adult clinical patients with confirmed COVID-19 (RT-PCR positive for SARS-CoV-2) at  
91 Helsinki University Hospital (HUU) (hospitalized: n = 34; outpatients: n = 8) were enrolled in  
92 the present study. Blood samples were collected during hospitalization for the severe COVID-  
93 19 group, and after confirmation of diagnosis for the mild COVID-19 outpatient group.  
94 Samples for RNA sequencing were collected in 2020 and representing infections by the original  
95 and early SARS-CoV-2 variants, whereas samples for *ex vivo* culture experiments were  
96 collected in 2021-2022 likely representing infections by omicron subvariants of SARS-CoV-  
97 2. As controls, healthy blood donors were included for RNA sequencing (n = 7, age  $57 \pm 7$ ,  
98 male/female 3/4) and *ex vivo* culturing experiments (n = 9, age  $38 \pm 14$ , male/female 4/5). The  
99 study was approved by the Ethics Committee of the Hospital District of Helsinki and Uusimaa  
100 (HUS/853/2020, HUS/1238/2020). All volunteers gave a written informed consent, in  
101 accordance with the Declaration of Helsinki. For clinical correlation analysis, severe COVID-  
102 19 patients were further categorized by severity based on their need for hospitalization and  
103 oxygen supplementation, as described previously <sup>7</sup>. For each patient, medical history and  
104 clinical data were collected through retrospective patient record review and are presented for  
105 the severe COVID-19, hospitalized patients in Table 1 and as previously described <sup>7</sup>.  
106 Calprotectin was measured from serum (diluted 1:1000) by ELISA, according to the  
107 manufacturer's protocol (calprotectin/S100A8 DuoSet kit, R&D systems).

### 108 **Isolation of granulocytes from human blood**

109 Blood samples from COVID-19 patients and healthy controls (HC) were collected in EDTA  
110 vacutainer tubes and transported to the laboratory. Peripheral blood mononuclear cells

111 (PBMCs) or polymorphonuclear cells (PMNs) were isolated from whole blood by density  
112 gradient centrifugation using either Ficoll-Paque Plus (GE Healthcare) or Polymorphprep  
113 (Axis-Shield) respectively, following standard procedures including the use of 2 mM EDTA in  
114 PBS and red blood cell lysis with ACK lysis buffer (Lonza by Thermo Fisher). Subsequently,  
115 isolation of CD66<sup>+</sup> granulocytes (low-density granulocytes, LDGs) from the PBMC fraction  
116 was performed using the CD66abce MicroBead Kit (Miltenyi Biotec, Germany) with an MS  
117 column, according to the manufacturer's instructions. Both the positively selected CD66<sup>+</sup>  
118 LDGs and the isolated PMNs were then washed and counted, using a TC20<sup>TM</sup> Automated Cell  
119 Counter (Bio-Rad Laboratories, Inc.) with trypan blue staining for dead cell exclusion. All  
120 described procedures in this section were done at room temperature. An aliquot of cells was  
121 lysed in Trizol reagent (Thermo Fisher Scientific, USA) and stored at  $-80^{\circ}\text{C}$  for later extraction  
122 of total RNA and subsequent RNA sequencing (RNA-seq) analysis.

### 123 **Caspase1 activity**

124 Caspase1 activity was assessed in isolated cells after 2 h of culture (1 million cells/ml) using  
125 the caspase-Glo<sup>®</sup>1 inflammasome assay (Promega) according to the manufacturer's protocol,  
126 with 2.5  $\mu\text{M}$  nigericin (Invivogen) treatment as the activator. The resulting luminescence was  
127 measured by a Hidex Sense microplate reader (Hidex).

### 128 **Soluble factor stimulation assays**

129 Isolated granulocytes from HC and COVID-19 patients were cultured at 2 million cells/ml in  
130 RPMI 1640 supplemented with 10% fetal bovine serum (R10) at  $37^{\circ}\text{C}$ . Cells were primed (1<sup>st</sup>  
131 signal) with either LPS (20 ng/ml, Sigma Aldrich) or IFN-I (combination of  $2.7 \times 10^4$  IU/ml  
132 IFN- $\alpha$  and IFN- $\beta$ , Immunotools) for 4 h, followed by activation (2<sup>nd</sup> signal) by 2.5  $\mu\text{M}$  nigericin  
133 or monosodium urate crystals (MSU, 100  $\mu\text{g}/\text{ml}$ , Invivogen) for an additional 4 h. For the 24  
134 h stimulation experiments, nigericin was added to the cultured cells, in the presence or absence

135 of inflammasome inhibitors MCC995 (2 µg/ml) and Ac-YVAD-FMK (20 µg/ml, both from  
136 Invivogen). Cells were pelleted by centrifugation at 400 G for 5 min and stored in Trizol at –  
137 80°C for later RNA extraction whereas supernatants were used to measure IL-1β, IL-18,  
138 myeloperoxidase (MPO) and IL-8 by ELISAs according to the manufacturer’s protocols  
139 (DuoSet kits from R&D systems). LDH was measured in supernatants using Cyquant LDH  
140 cytotoxicity assay (ThermoFisher). HL-60 cells (ATCC #CCL-240) were activated similarly  
141 to neutrophils after a 5-day differentiation period induced by 1 % DMSO.

142

### 143 **Virus propagation**

144 The SARS-CoV-2 hCoV-19/Finland/THL-202117309/2021 (delta strain B.1.617.2) and the  
145 mouse-adapted strain MaVie<sup>18</sup> were propagated in VeroE6-TMPRSS2 cells (kidney epithelial  
146 cells expressing the transmembrane protease serine 2)<sup>19</sup> grown in DMEM supplemented with  
147 10% inactivated FCS, 100 IU/mL Penicillin, 100 µg/mL Streptomycin and 2 mM L-glutamine  
148 at 37°C. The virus was purified from supernatants by ultracentrifugation (SW28 rotor, 27,000  
149 rpm, 90 min, +4 °C) through a 0.22 µm-filtered 30% ultra-pure sucrose cushion (in PBS), to  
150 obtain virus preparations free of cell culture contaminants. Virus titers were calculated by the  
151 median tissue culture infectious dose (TCID<sub>50</sub>) after assessing cytopathic effects by crystal  
152 violet staining of cell cultures infected for 5 days with serially diluted virus.

153

### 154 **RNA sequencing**

155 Neutrophils isolated from different cohorts comprised three PMN groups (severe COVID-19,  
156 mild COVID-19, and healthy controls), and one LDG group (given that these cells were rare  
157 in mild COVID-19 patients and HC, only LDGs from patients with severe COVID-19 were  
158 included).

159 cDNA synthesis from total RNA was performed according to Takara SMARTseq v4 Ultra-low  
160 input RNA kit for Sequencing user manual (Takara Bio, Mountain View, CA, USA) followed  
161 by Illumina Nextera XT Library preparation according to Illumina Nextera XT Reference  
162 Guide (Illumina, San Diego, CA, USA). UDI index setup was used for the Nextera XT libraries.  
163 Library quality check was performed using LabChip GX Touch HT High Sensitivity assay  
164 (PerkinElmer, USA) and libraries were pooled based on the concentrations acquired from the  
165 assay. The pooled libraries were quantified for sequencing using KAPA Library Quantification  
166 Kit (KAPA Biosystems, Wilmington, MA, USA) and sequenced on the Illumina NovaSeq6000  
167 system for 200 cycles using S1 flow cell (Illumina, San Diego, CA, USA). Read length for the  
168 paired-end run was 2x101 bp.

169

#### 170 **RNA data analysis**

171 Principal Component Analysis (PCA) was performed on the normalized gene expression  
172 matrix using the Chipster software <sup>20</sup> to identify patterns in the data and reduce the  
173 dimensionality of the dataset. The top principal components were selected based on the  
174 percentage of variance explained. For enrichment analyses, Gene Set Enrichment Analysis  
175 (GSEA) and Over-Representation Analysis (ORA) were performed on the top 5000 DE genes  
176 identified by DESeq2 (adjusted P value < 0.05, log<sub>2</sub>FC >1) using ExpressAnalyst <sup>21</sup>. GSEA  
177 was used to identify enriched signaling pathways using the Reactome database, while ORA  
178 was used to identify enriched pathways using the KEGG database. The resulting p-values were  
179 corrected for multiple testing using the Benjamini-Hochberg method, and pathways with a  
180 corrected p-value <0.05 were considered significant.

181 To visualize the expression patterns of the differentially expressed (DE) genes, the data was  
182 analyzed using the AltAnalyze software <sup>22</sup>, which selected the top 95 genes based on correlation  
183 and determined the heatmap clustering, using the Euclidean distance metric and the complete

184 linkage method. Then, the obtained heatmap was re-generated using `heatmapper.ca`<sup>23</sup> for better  
185 visualization.

186 CIBERSORTx, a machine learning algorithm that infers cell type proportions using a reference  
187 gene expression matrix of known cell types (25) was used to perform RNA-seq deconvolution  
188 on the gene expression data to estimate the abundance of immune cell types in the samples<sup>24</sup>.  
189 The signature matrix used was taken from Lasalle *et al.*<sup>8</sup>. This reference matrix made use of a  
190 published whole-blood single-cell dataset<sup>9</sup>, and included the main immune cell types:  
191 monocytes, NK cells, T lymphocytes, B lymphocytes, plasmablasts and neutrophils, the latter  
192 subclassified into mature and immature. The smaller subsets of granulocytes (eosinophils and  
193 basophils) are not considered separately and are most likely categorized as neutrophils in the  
194 bulk data deconvolution. Nonetheless, the resulting cell type proportions were used to compare  
195 the immune cell composition between groups.

196 Additionally, the determination of sample purity (>80% of “mature neutrophils” for PMNs or  
197 “immature neutrophils” for LDGs) served as a limiting parameter for the visualization of  
198 differentially expressed inflammasome related genes from the RNA sequencing results, which  
199 were selected and graphed in a heatmap using `heatmapper.ca`<sup>23</sup>, clustered by complete linkage  
200 and ordered by Spearman’s rank.

201

## 202 **Volcano Plots**

203 To visualize differentially expressed (DE) genes between groups from human and mice RNA-  
204 seq results previously identified by DESeq2, a volcano plot was generated using GraphPad  
205 Prism. Genes with a P-adjusted value (*padj* or FDR) <0.05 were considered significant.  
206 Similarly, RNA sequencing data from GSE93996<sup>25</sup> was reanalyzed, and all DE genes in  
207 ATRA-differentiated HL-60 cells were visualized in a volcano plot.

208

## 209 **Single cell transcriptomics data analysis**

210 This study made use of the “COVID-19 Immune Atlas: integration of 5 public COVID-19  
211 PBMC single-cell datasets” available online<sup>26</sup>. This standardized data collection contains cells  
212 from different assays (10x 3' v2, 10x 3' v3, 10x technology and Seq-Well) and consists of a  
213 total of 239,696 cells from the peripheral blood, 3,693 of which are neutrophils. These  
214 neutrophils were further subclassified as mature (59%) and immature (41%), based on the  
215 immune atlas predetermined cell classes. This was confirmed by a CD16b expression in mature  
216 neutrophils, and a higher CD66b expression in the immature population. This data was obtained  
217 from and analyzed in the Chan Zuckerberg CELLxGENE platform<sup>26</sup>.

218

## 219 **Reverse transcription and quantitative PCR (RT-qPCR) for human selected human** 220 **genes**

221 Total RNA was extracted from unstimulated or *ex vivo* stimulated PMNs using the Trizol  
222 reagent (Invitrogen, USA) according to the manufacturer’s protocol. Subsequently, cDNA  
223 synthesis was performed using the RevertAid RT Reverse Transcription Kit (Thermo  
224 Scientific, USA) as per the manufacturer's instructions. Quantitative PCR (qPCR) was  
225 performed using the Stratagene model (Agilent Technologies) and SYBR Green/ROX master  
226 mix (Thermo Scientific, USA). The primer sequences for qPCR are presented in  
227 Supplementary Table S1.

228 Primer specificity was confirmed using melting curve analysis and dissociation curves. The  
229 relative expression levels of the genes of interest were calculated using the  $2^{-\Delta\Delta CT}$  method  
230 and normalized to the expression of the housekeeping gene GAPDH. Baseline gene expressions  
231 of unstimulated samples were statistically assessed using the Mann-Whitney test, while the  
232 two-way ANOVA Tukey’s multiple comparisons test was performed for the *ex vivo* stimulated  
233 samples.

## 234 **Mouse infections**

235 Experimental procedures were approved by the Animal Experimental Board of Finland (license  
236 number ESAVI/28687/2020). Female BALB/c mice (Envigo, Indianapolis, IN, USA; 7 to 8  
237 weeks, n = 36 in total) were transferred to the University of Helsinki biosafety level-3 (BSL-  
238 3) facility and acclimatized to individually ventilated biocontainment cages (ISOcage;  
239 Scanbur, Karl Sloanestran, Denmark) for 7 days with *ad libitum* water and food (rodent pellets).  
240 For subsequent experimental infection, the mice were placed under isoflurane anesthesia and  
241 inoculated intranasally with 50  $\mu$ L of SARS-CoV-2 MaVie strain ( $5 \times 10^5$  TCID<sub>50</sub>/animal) or  
242 PBS (mock-infected control). Daily weighting of all mice was performed, and their well-being  
243 was carefully monitored for signs of illness (e.g., changes in posture or behavior, rough coat,  
244 apathy, ataxia). Euthanasia was performed by cervical dislocation under terminal isoflurane  
245 anesthesia. All animals were dissected immediately after euthanasia, and the lungs were  
246 sampled for multiple downstream analyses. The infections were performed as 3 separate  
247 experiments (exp) with 12 mice each: 1) Exp 1 included 8 mice infected with MaVie and 4  
248 mock infected mice. At 2 days post infection (dpi), 4 infected and the mock infected mice were  
249 euthanized; the remaining infected mice were euthanized at 4 dpi. The right lung was sampled  
250 for virus-specific RT-qPCR (1/5) and neutrophil isolation (4/5), the left lung was fixed for  
251 histological and immunohistochemical examination. 2) Exp 2 included 8 infected and 4 mock  
252 infected mice of which half were euthanized at 2 dpi and 4 dpi, respectively. From these mice,  
253 both lung lobes were subjected to neutrophil isolation. 3) Exp 3 included 8 mice that were  
254 infected and immediately inoculated intraperitoneally with 250  $\mu$ g of anti-mouse IFNAR-1 (n  
255 = 4) or IgG1 isotype control (n = 4) (Bio-X-Cell, New Hampshire, USA), and 4 mock-infected  
256 animals. All mice were euthanized at 2 dpi. Each 1 1/5 of the left lobe was processed for virus-  
257 specific RT-qPCR and histology and immunohistochemistry respectively. The remaining  
258 approx. 80% of the lungs served for neutrophil isolation.

## 259 **Neutrophil isolation from mouse lungs**

260 Neutrophil isolation was performed from the lungs of all mice. The dissected lung tissue was  
261 chopped into small pieces using scissors and enzymatically digested with a cocktail of Liberase  
262 (50 ug/ml; Roche #05401020001 from Merck) and DnaseI (100 ug/ml; Roche #11284932001  
263 from Merck) in RPMI-1640 for 30 min at 37 °C. The resulting homogenate was diluted 10-  
264 fold in R10 and passed through a 70 µm Cell strainer (Pluriselect) to obtain a single-cell  
265 suspension. Neutrophils were isolated by positive selection using Ly6G-binding magnetic  
266 beads and MS columns according to the manufacturer's recommendations (Miltenyi Biotec).  
267 Neutrophils were isolated with a purity exceeding 95% based on flow cytometry analysis of  
268 Ly6G expression.

269

## 270 **RNA sequencing of mouse neutrophils**

271 Mouse neutrophils were isolated, lysed in Trizol (Thermo Scientific) and the RNA extracted  
272 in the liquid phase using chloroform. RNA isolation was carried out using the Rneasy micro  
273 kit (Qiagen). Isolated RNA (1 ng) underwent whole transcriptome sequencing with  
274 ribodepletion. Briefly, RNA sequencing was performed using the Illumina Stranded with  
275 RiboZero library preparation method. Sample quality and integrity were assessed using  
276 TapeStation RNA analysis. Sequencing was conducted on the Illumina NextSeq platform,  
277 followed by standard bioinformatics analysis for gene expression quantification.

278 The service was provided by the Biomedicum Functional Genomics Unit at the Helsinki  
279 Institute of Life Science and Biocenter Finland at the University of Helsinki.

280

## 281 **RT-qPCR of mouse samples**

282 RNA was extracted from dissected lung samples (1/10 of the whole lung) of mice in Exp 1 and  
283 Exp 3 as well as isolated neutrophils using Trizol (Thermo Scientific) following the



284 manufacturers' instructions. The isolated RNA was directly subjected to one-step RT-qPCR  
285 analysis based on a previously described protocol using primer-probe sets detecting the viral  
286 genome encoding for the RNA-dependent RNA polymerase (RdRp)<sup>27</sup>, subgenomic E<sup>28</sup> as  
287 well as mouse caspase1, IL1b and GAPDH (Applied biosystems #Mm00438023\_m1,  
288 #Mm00434228\_m1 and #Mm99999915\_g1 respectively, Thermo scientific). The PCRs were  
289 performed with TaqPath 1-step master mix (ThermoFisher Scientific) using AriaMx  
290 instrumentation (Agilent, Santa Clara, CA, USA).

291

### 292 **Histology and immunohistochemistry**

293 From animals in Exp 1 and Exp 3 the whole left lung (Exp 1) or 1/5 of the left lung (Exp 3)  
294 were trimmed for histological examination and routinely paraffin wax embedded. Consecutive  
295 sections (3 µm) were prepared and routinely stained with hematoxylin-eosin (HE) or subjected  
296 to immunohistochemistry (IHC) for the detection of SARS-CoV-2 nucleoprotein (NP)<sup>29</sup> and  
297 Ly6G (neutrophil marker); for Exp 3, a further section of the infected lungs was stained for  
298 histone H3 (NET marker)<sup>30</sup>. All stains followed previously published protocols<sup>31</sup>.

299

### 300 **Morphometric analyses**

301 For quantification of SARS-CoV-2 antigen expression and the extent of neutrophil influx into  
302 the lungs, a morphometric analysis was undertaken on the slides stained for SARS-CoV-2 NP  
303 and Ly6G, respectively. The stained slides were scanned using NanoZoomer 2.0-HT  
304 (Hamamatsu, Hamamatsu City, Japan), and several sections of the lung of each animal were  
305 quantitatively analysed using the Visiopharm 2022.01.3.12053 software (Visiopharm,  
306 Hoersholm, Denmark). The morphometric analysis served to quantify the area, in all lung  
307 sections of an animal, that showed immunostaining for viral NP and Ly6G, respectively. In  
308 Visiopharm, for each section, the lung was manually outlined and annotated as a Region Of

309 Interest (ROI), manually excluding artifactually altered areas. The manual tissue selection was  
310 further refined with an Analysis Protocol Package (APP) based on a Decision Forest classifier,  
311 with the pixels from the ROI being ultimately classified as either “Tissue” or “Background”.  
312 This new “Tissue” ROI, regrouping the different lung samples analysed for each animal, was  
313 further quantified by executing two APPs successively. The first APP was based on a Threshold  
314 classifier and served to detect and outline areas with immunostaining. The second APP then  
315 measured both the surface of the immunostained area ( $\mu\text{m}^2$ ) and the surface of the “Tissue”  
316 ROI ( $\mu\text{m}^2$ ). The percentage of immunostained area (%), expressed as the ratio between the  
317 immunostained area and the total area, was obtained for each animal in Excel (Microsoft Office  
318 2019; Microsoft, Redmond, Washington, United States), according to the following formula:  
319 
$$([\text{positive area } (\mu\text{m}^2)] / [\text{total area } (\mu\text{m}^2)]) \times 100.$$

320

### 321 **Statistical analyses**

322 Statistical analysis was performed using GraphPad Prism 8.3 software (GraphPad Software,  
323 San Diego, CA, USA) and R software v3.6.3 (R core team). Statistically significant correlations  
324 between parameters were assessed by calculating Spearman’s correlation coefficients, and  
325 differences between groups were assessed with Mann-Whitney, Kruskal-Wallis or ordinary  
326 one-way or 2-way ANOVA tests, depending on sample distribution and the number of groups  
327 analyzed.

## 328 **Results**

### 329 **Unsupervised RNA-seq analysis reveals a gene expression signature of circulating** 330 **neutrophils in COVID-19 that is strongly influenced by maturity**

331

332 With our recent findings on increased frequencies of low-density granulocytes (LDGs, isolated  
333 from the PBMC fraction) during COVID-19 and their likely relevant role in disease progression  
334 <sup>7</sup>, we sought to understand in more detail how the transcriptomic profile of LDGs differs from  
335 their higher “normal” density counterpart, the circulating polymorphonuclear cells (PMNs) <sup>32</sup>,  
336 typically consisting mainly of mature neutrophils. Neutrophils isolated from different cohorts  
337 comprised three PMN groups (severe COVID-19, mild COVID-19, and healthy controls), and  
338 one LDG group. We explored gene expression through RNA sequencing (RNA-seq) and  
339 confirmed the distinctive gene signature of LDGs by principal component analysis (PCA)  
340 (Figure 1A), which revealed that the gene expression patterns of COVID-19 LDGs differed  
341 from those of all PMNs regardless of the patients’ disease state.

342 Functional enrichment analyses through gene overrepresentation and gene-set enrichment  
343 analyses (ORA and GSEA, respectively) compared LDGs with PMNs from severe COVID-19  
344 patients (Figure 1B). When considering the top 5000 differentially expressed genes (DEG),  
345 DNA replication and cell cycle were the most overrepresented pathways identified by ORA  
346 (Figure 1B), which supported our previous findings suggesting LDGs to be predominantly  
347 immature cells <sup>7</sup>. However, the next statistically significant result was an underrepresentation  
348 of the NLR signaling pathway genes in LDGs in contrast with PMNs, highlighting that LDGs  
349 have an inflammatory profile that differs from that of PMNs, also depicted in the GSEA (Figure  
350 1B). Briefly, type I and II interferon signaling were among the most significantly enriched gene  
351 sets in PMNs compared to LDGs. Further analysis showed that PMNs from severe COVID-19  
352 patients had significantly enriched DEGs in inflammatory pathways such as NLR, tumor

353 necrosis factor (TNF), retinoic acid-inducible gene-I (RIG-I) like, autophagy, MAPK and  
354 JAK/STAT signaling pathways compared to either HC PMNs or severe COVID-19 LDGs  
355 (Supplementary Fig. 1A-D). Interestingly, many of the observed DEGs were linked to  
356 inflammasome formation (Supplementary Fig. 1E-F). However, mild COVID-19 PMNs did  
357 not significantly differ from HC PMNs in their inflammatory profile (Supplementary Fig. 1G-  
358 H).

359 Additionally, we performed unsupervised Iterative Clustering and Guide Gene Selection  
360 (ICGS), which identified the top DEGs and classified the samples into two major clusters: a  
361 first one containing all isolated LDG samples, and a second one comprising all isolated PMN  
362 samples (Figure 1C). The former cluster consisted of many neutrophil marker genes (e.g.  
363 *CEACAM8*, *MMP8*, *DEFA*), while in the latter cluster the most significantly upregulated genes  
364 in the severe COVID-19 subgroup were mainly interferon inducible (e.g. *OAS1*, *OAS2*, *IFI44L*,  
365 *IFITM3*, *IFIT2*) as well as some inflammasome related (*CASP5*, *CARD16*) genes.

366

367

### 368 **Mature neutrophils from severe COVID-19 display a strong IFN-related gene expression** 369 **signature**

370 To gain a comprehensive understanding of the cellular composition within PMN and LDG  
371 fractions, we performed a deconvolution of the RNA-seq data, which verified that most cells  
372 present in the samples were neutrophils. This analysis also demonstrated that cells in the LDG  
373 fraction were predominantly immature neutrophils, meanwhile PMNs were composed of  
374 mainly mature neutrophils (Figure 2A). Subsequently, gene expression analysis of PMNs and  
375 LDGs containing high purity of mature neutrophils and immature neutrophils (over 80%),  
376 respectively, confirmed that mature neutrophils from severe COVID-19 displayed an increased

377 expression of type I IFN related genes, while immature neutrophils from severe COVID-19  
378 distinctively lacked this signature (Figure 2B).

379

380 **Inflammasomes are activated in severe COVID-19 PMNs, but not directly by SARS-CoV-**  
381 **2**

382 Looking more closely into PMN fractions, ORA identified the inflammasome related NOD-  
383 like and RIG-like receptor signaling pathways among the most significantly overrepresented  
384 pathways, differentially expressed in severe COVID-19 PMNs versus HC PMNs (Figure 3A)  
385 or mild COVID-19 PMNs (Figure 3B). The increased expression of selected IFN-I (*OAS1*,  
386 *OAS2*, and *IFIT1*) and inflammasome related genes (*CASP1*, *CASP5*, *NLRC5* and *NAIP*) was  
387 confirmed by RT-qPCR. However, some inflammasome related genes (*IL-1 $\beta$* , *NLRP3* and  
388 *NLRC4*) were seemingly downregulated, although not statistically significant (Supplementary  
389 Fig. 2).

390 Given the strong upregulation of many inflammasome related genes during severe COVID-19,  
391 we assessed whether PMNs exhibit active inflammasome formation *in vivo*. To evaluate  
392 spontaneous inflammasome mediated cytokine secretion, fresh PMNs isolated from severe  
393 COVID-19 patients and HC were cultured *ex vivo* overnight. We measured the levels of IL-1 $\beta$   
394 and IL-18 in the supernatant and found that IL-1 $\beta$  secretion was significantly increased in the  
395 supernatant of severe COVID-19 PMNs compared to HC PMNs (Figure 3C), whereas the IL-  
396 18 levels did not differ significantly (Figure 3D). Additionally, since SARS-CoV-2 viral  
397 particles were previously implicated to induce inflammasome formation in macrophages<sup>17</sup>, the  
398 IL-1 $\beta$  and IL-18 levels after HC PMNs exposure to SARS-CoV-2 were also assessed but no  
399 significant effects in the secretion of these cytokines were observed (Figure 3E, F).

400 The spontaneous secretion of IL-1 $\beta$  by COVID-19 PMNs suggests that these cells are actively  
401 producing and releasing IL-1 $\beta$  through inflammasome formation which is dependent on  
402 caspase1 activity<sup>33</sup>. We assessed caspase1 activity in response to the second signal required  
403 for inflammasome activation, induced by nigericin, and observed increased caspase1 activity  
404 in severe COVID-19 PMNs compared to HC PMNs (Figure 3G). These findings suggest that  
405 severe COVID-19 PMNs have an increased capacity for inflammasome activation, potentially  
406 due to an existing priming signal during acute disease *in vivo*. However, no significant  
407 difference in caspase1 activity between non-exposed and virus-exposed PMNs were observed  
408 (Figure 3G), indicating that caspase1 activation in COVID-19 PMNs is not directly triggered  
409 by the virus.

410

411 **Activation of neutrophil inflammasome related pathways during respiratory distress is**  
412 **not specific to COVID-19**

413 We also reanalyzed the RNA-seq data previously generated by LaSalle *et al.*<sup>8</sup>, focusing on  
414 neutrophil transcriptomics in patients with COVID-19 as compared to non-COVID-19 patients  
415 exhibiting similar respiratory symptoms, as well as to healthy controls. Our analysis included  
416 IFN- $\alpha$  response, IL-1 $\beta$  production, TLR signaling, NLRP3 inflammasome, and pyroptosis  
417 pathways, using the Gene Ontology (GO) database; the NLR signaling pathway using the  
418 Kyoto Encyclopedia of Genes and Genomes (KEGG) database; and inflammasome pathway  
419 using the REACTOME database (Figure 4). These pathways were significantly enriched in  
420 COVID-19 patients, supporting our findings. Importantly, the genes from the above-mentioned  
421 pathways were also induced in non-COVID-19 patients, suggesting that these pathways  
422 represent a general neutrophil response to inflammatory stimuli rather than a COVID-19  
423 specific response.

424

## 425 **Type I IFNs prime PMNs for inflammasome activation**

426 Since PMNs from COVID-19 patients concomitantly display a strong IFN-I signature (Figure  
427 2B) and an increased propensity for inflammasome activation, we hypothesized that IFN-I  
428 could act as the priming signal for PMN inflammasomes during COVID-19. Isolated HC PMNs  
429 were stimulated *ex vivo* with exogenous IFN-I and the well-described inflammasome priming  
430 (1<sup>st</sup> signal) and activator (2<sup>nd</sup> signal) agents LPS and nigericin, respectively <sup>34,35</sup>. After  
431 stimulation, both priming signals induced pro-IL-1 $\beta$  (31 kDa) in the cell lysates, followed by  
432 the release of active IL-1 $\beta$  (17 kDa) into the supernatant in response to nigericin (Figure 5A),  
433 confirming the ability of IFN-I to prime PMNs for inflammasome activation.

434 To assess inflammasome formation in circulating neutrophils during COVID-19, PMNs from  
435 HC and COVID-19 patients underwent similar stimulation assays as above, followed by IL-1 $\beta$   
436 measurement from supernatants by ELISA. In addition, to further assess the role of SARS-  
437 CoV-2 virus particles in neutrophil inflammasome activation, HC PMNs were cultured in the  
438 presence of purified viruses (10 infectious units/PMN). HC PMNs responded to both LPS and  
439 IFN-I by increasing their IL-1 $\beta$  secretion, which was exponentiated after exposure to nigericin  
440 (Figure 5A), confirming the ability of IFN-Is to prime for inflammasome assembly in PMNs,  
441 albeit less efficiently than LPS. Interestingly, COVID-19 PMNs produced less IL-1 $\beta$  than HC  
442 PMNs upon exogenous inflammasome activation primed by either LPS or IFN-I, while SARS-  
443 CoV-2 particles did not have any effect on PMN inflammasome activation (Figure 5B). As  
444 with 24-h cultures (Figure 3D), we did not detect any significant changes in IL-18 expression  
445 in either HC or COVID-19 PMNs (data not shown). However, myeloperoxidase (MPO), a  
446 marker of neutrophil degranulation and NETosis <sup>36</sup>, responded to nigericin indistinctively  
447 between COVID-19 PMNs and HC PMNs, and therefore the observed diminished IL-1 $\beta$   
448 release by COVID-19 PMNs is not due to general cellular inertia but may be specific to the *ex*

449 *vivo* induced inflammasome pathway. Furthermore, additional stimulation assays in the  
450 presence of the NLRP3 inhibitor MCC950 (Figures 5D-E) and caspase1 inhibitor YVAD  
451 (Supplementary Fig. 3A) confirmed that induced IL-1 $\beta$  secretion is dependent on canonical  
452 NLRP3 inflammasome activation. However, unlike IL-1 $\beta$  (Supplementary Fig. 3B), increased  
453 IL-18 secretion was not detectable even after 24-h stimulation (Supplementary Fig. 3C).  
454 Furthermore, the observed residual IL-18 was not affected by inflammasome inhibitors,  
455 suggesting its secretion to be unrelated to inflammasome activity in PMNs.

456 We further assessed the specificity of inflammasome activation by measuring LDH and IL-8  
457 levels in the supernatants from the same cells and under the same experimental conditions as  
458 shown in Figures 5D-E. The measurements of the former were done to assess inflammasome  
459 mediated cell death by pyroptosis in response to nigericin, while the latter was assessed to  
460 demonstrate the responsiveness of PMNs to an inflammasome unrelated inflammatory cascade.  
461 As with IL-1 $\beta$  secretion, COVID-19 PMNs were less responsive than HC PMNs to nigericin-  
462 and LPS-mediated LDH (Figure 5F) and IL-8 (Figure 5G) release, respectively. This suggests  
463 that COVID-19 PMNs are generally poorly responsive to inflammatory stimuli while retaining  
464 the ability for degranulation and NETosis (see above).

465 To examine this reduced responsiveness to external inflammatory priming, we evaluated the  
466 inflammasome related gene expression following *ex vivo* stimulation with IFN-I or LPS (Figure  
467 5H-I and Supplementary Fig. 3D-G). OAS1 gene, an interferon stimulated gene (ISG), showed  
468 significant upregulation by IFN-I in COVID-19 PMNs as compared to HC PMNs (Figure 5H),  
469 while the inflammasome related genes IL-1 $\beta$  (Figure 5I), CASP1 (Figure 5J) and NLRC5  
470 (Figure 5K) were more efficiently induced in HC PMNs than COVID-19 PMNs. This suggests  
471 that the inflammasome defect in COVID-19 PMNs is at the transcriptional level when using



472 IFN-I as the priming factor, while high OAS1 gene expression indicates transcriptional defect  
473 is restricted to individual genes.

#### 474 **Association between *ex vivo* inflammasome activation and disease severity**

475 Our analysis of the association between *ex vivo* inflammasome activation (caspase1 activity  
476 and IL-1 $\beta$  release) and clinical markers of disease severity, including neutrophil responses,  
477 revealed intriguing links. Calprotectin is marker of neutrophil activation or death<sup>37</sup> but also  
478 potentially activates the inflammasome<sup>38</sup>. A significant positive correlation between  
479 calprotectin plasma levels and PMN caspase1 activity (Figure 6A-B) underscores this latter  
480 possibility and highlights the interplay between inflammation and inflammasome activation in  
481 PMNs of COVID-19 patients. Furthermore, the negative association of PMN IL-1 $\beta$  levels (after  
482 *ex vivo* stimulation) with disease severity (WHO ordinal scale, Figure 6A) and patient  
483 neutrophil counts (Figure 6A, C) supports the exhaustion hypothesis, wherein PMNs from  
484 severe COVID-19 patients may be less responsive to stimuli due to prior *in vivo* activation.  
485 While these findings provide intriguing insights into the complex interplay between  
486 calprotectin release, caspase1 activity, and inflammasome activation in COVID-19, additional  
487 research is required to further elucidate these connections.

#### 488 **LDGs differ from PMNs in gene expression and release of inflammasome related** 489 **interleukins**

490 To assess the inflammasome related inflammatory profile of COVID-19 LDGs in comparison  
491 to PMNs, we analyzed the differential expression of inflammasome related genes using RNA-  
492 seq (Figure 7A). LDGs differed significantly from PMNs, with the most striking difference  
493 being their increased expression of IL-18 and NLRC4, whereas PMNs displayed higher levels  
494 of IL-1 $\beta$ , NLRP3 and caspases 1, 4 and 5. Single cell sequencing data from the COVID-19

495 immune atlas confirmed our transcriptomic results (Figure 7B), from which a detailed gene by  
496 gene analysis of the most relevant inflammasome related genes is shown (Figure 7C and  
497 Supplementary Fig. 4). Briefly, PYCARD gene coding for the ASC protein was expressed  
498 similarly in mature and immature neutrophils (Supplementary Fig. 4), confirming that both cell  
499 types have inflammasome forming capacity. However, most of the inflammasome gene  
500 expressions differed significantly and in the same manner as in our transcriptomic analysis.

501

502 We conducted *ex vivo* stimulation assays using LDGs isolated from COVID-19 patients,  
503 similar to the approach used for PMNs described earlier. Like PMNs, IL-1 $\beta$  secretion by LDGs  
504 was elevated in the presence of a priming signal (IFN-I or LPS), which exponentially increased  
505 when the inflammasome activation signaling molecule nigericin was added (Figure 7D).  
506 Contrary to PMNs and in line with the transcriptomics data, an increased IL-18 secretion was  
507 detected (Figure 7E). Additionally, the secretion of both ILs by LDGs was inhibited in the  
508 presence of inflammasome specific inhibitors MCC950 and YVAD (Figure 7F-G).

509 These findings suggested that the outcome of neutrophil inflammasome activation varies based  
510 on cellular maturation state. To explore this further, we conducted *in vitro* stimulation studies  
511 using differentiated HL-60 cells, an immature neutrophil-like model<sup>39</sup>. Similar to LDGs from  
512 COVID-19 patients, HL-60 displayed comparable IL-18 secretion pattern upon LPS or IFN-I  
513 stimulation and nigericin-induced activation. Notably, their IL-1 $\beta$  release was only detected  
514 with LPS priming (Figures 7F-G). Furthermore, consistent with transcriptomic analysis  
515 revealing an upregulation of inflammasome related genes upon differentiation (Figure 7H), the  
516 capacity of HL-60 cells to secrete inflammasome related cytokines was differentiation-  
517 dependent (data not shown). Overall, these findings suggest that neutrophils may lose the  
518 ability to secrete IL-18 during maturation, and release of neutrophil-derived IL-18 occurs

519 primarily in disease states associated with extensive granulopoiesis and increased immature  
520 granulocyte counts in the blood, like COVID-19<sup>40</sup>.

521

### 522 **Neutrophils are recruited to the lungs in SARS-CoV-2 infected mice**

523 Hamsters and human ACE2 expressing mice infected with SARS-CoV-2 develop pulmonary  
524 inflammation including neutrophil recruitment<sup>41–43</sup>. To further assess the role of neutrophils in  
525 COVID-19, we utilized a recently developed SARS-CoV-2 mouse model<sup>18</sup>. This model  
526 employs the MaVie strain, serially passaged in mouse lungs and causing pneumonia similar to  
527 human COVID-19 in wild-type BALB-C mice<sup>18</sup>. Infected mice started losing weight by day 2  
528 post-infection, with some mice reaching the clinical endpoint of 20% weight loss by day 4  
529 (Supplementary Fig. 5A). Viral loads were significantly higher at 2 dpi than 4 dpi (Figure 8A),  
530 and viral antigen expression, widespread at 2dpi in bronchioles and alveoli, matched this  
531 pattern (Figure 8B and D). The extensive viral replication at 2 dpi was associated with  
532 degeneration of infected epithelial cells, most prominent in the respiratory epithelium,  
533 accompanied by neutrophil (Ly6G+) infiltration (Figure 8D) and a significant increase in the  
534 number of neutrophils in the lungs of infected mice compared to PBS-inoculated mice (Figure  
535 8C). Neutrophil numbers significantly decreased by 4dpi but remained higher than controls  
536 (Figure 8C). Detailed information on the histological and immunohistochemical features of  
537 these mice is provided in Supplementary Table S2. Together, these findings suggest a pivotal  
538 role of neutrophils in clearing the virus in SARS-CoV-2 infected mice.

539

### 540 **Neutrophils from SARS-CoV-2 infected mice display IFN-I dependent caspase1** 541 **activation**

542 We isolated neutrophils from the lungs of infected mice at 2 and 4 dpi, as well as from non-  
543 infected mice (inoculated with PBS) for transcriptomic analysis by RNA-seq (Exp 1). PCA

544 showed distinct differences between neutrophils from infected and non-infected mice, with  
545 slight variation between the 2 and 4 dpi time points (Figure 9A). These differences were  
546 reflected in many DEGs, including several IFN-I responsive and inflammasome related genes,  
547 which showed strong upregulation at 2 dpi with slightly lower but still significantly elevated  
548 levels at 4 dpi, compared to non-infected mice (highlighted in the DEG heatmap; Figure 9B).  
549 The volcano plot (Figure 9C) provided a comprehensive view of the DEG pattern between  
550 neutrophils from SARS-CoV-2 infected and mock-infected mice. In addition to confirming the  
551 upregulation of IFN-I responsive and inflammasome related genes observed in the heatmap,  
552 the plot revealed a broader transcriptional response to viral infection with several additional  
553 DEG.

554 Next, we investigated if neutrophils from SARS-CoV-2 infected mice showed increased  
555 inflammasome formation, similar to PMNs from COVID-19 patients. Neutrophils from  
556 infected mice, harvested at 2 and 4 dpi, displayed increased caspase1 activity upon nigericin  
557 stimulation, compared to neutrophils from non-infected mice (Exp 2; Figure 9D). To assess the  
558 role of IFN-I, we inoculated mice with an IFN-I blocking anti-IFNAR monoclonal antibody or  
559 an isotype control antibody post-infection (Exp 3). Remarkably, neutrophils from anti-IFNAR  
560 treated mice showed diminished nigericin-induced caspase1 activity (Figure 9E). Furthermore,  
561 caspase1 and IL-1 $\beta$  gene expressions were lower in anti-IFNAR treated than isotype treated  
562 mice (Figure 9F-G). Taken together, IFN-I appears to be responsible for the increased caspase1  
563 activity in neutrophils of infected mice.

564 Histology of isotype-treated mice and anti-IFNAR treated mice lungs showed comparable  
565 features (Supplementary Fig. 5C) as infections without antibody (Exp 1; Figure 8B-D).  
566 Regardless of treatment, some neutrophils in infected mice displayed degeneration and  
567 NETosis evidenced by histone H3 staining (Supplementary Fig. 5C; Supplementary Table S2),  
568 and viral loads remained consistent between anti-IFNAR or IgG1 isotype control treated mice

569 (Supplementary Fig. 5B). Taken together, blocking IFN-I signaling did not alter virus  
570 replication, virus-induced pathological changes, or early neutrophil recruitment following  
571 infection.

## 572 Discussion

573 Neutrophils, the largest cell population of the host immune system, are rapidly recruited to sites  
574 of infection and play an important role in orchestrating an early immune response <sup>44,45</sup>. The  
575 relevance of neutrophils in viral infections became increasingly apparent during the COVID-  
576 19 pandemic, as they have been shown to be key mediators of the observed pathological  
577 processes <sup>46</sup>.

578 This study sheds light on the potential involvement of the inflammasome pathway in COVID-  
579 19, particularly by demonstrating its activation in neutrophils during SARS-CoV-2 infection.  
580 Our investigation of the inflammatory profile of neutrophils as the dominant population of  
581 peripheral blood polymorphonuclear cells (PMNs) revealed an increased ability of neutrophils  
582 from severe COVID-19 patients for inflammasome assembly as evidenced by their  
583 transcriptional profile, spontaneous release of IL-1 $\beta$ , and elevated caspase1 activity. These  
584 findings are consistent with previous reports indicating activation of the NLRP3 inflammasome  
585 and ASC specks in circulating neutrophils during acute COVID-19 <sup>14,16</sup>. Furthermore, despite  
586 showing increased caspase1 activity, neutrophils from COVID-19 patients exhibited  
587 diminished soluble IL-1 $\beta$  production upon exogenous activation of the NLRP3 inflammasome  
588 pathway compared to healthy controls, which suggests that this pathway is “exhausted” due to  
589 prior activation during the disease. Mechanistically, our findings show that IFN-I, elevated in  
590 COVID-19 patients <sup>47,48</sup>, can prime inflammasome formation in neutrophils. Transcriptomic  
591 analyses revealed that circulating neutrophils during severe COVID-19 show increased  
592 expression of IFN-responsive genes, suggesting inflammasome priming by IFN-I also *in vivo*  
593 during COVID-19 <sup>49</sup>. Furthermore, the study found that immature neutrophils, which are  
594 prevalent in low-density granulocyte fraction (LDGs), exhibit unique inflammasome gene  
595 expression and outcomes compared to mature neutrophils (PMNs). LDGs release IL-18 and

596 upregulate distinct inflammasome related genes but lack the IFN-I signature seen in PMNs  
597 during COVID-19, indicating lower responsiveness to IFN-I, and supported by less efficient  
598 IFN-I mediated inflammasome priming of LDGs *ex vivo*.

599 SARS-CoV-2 infected mice also showed increased neutrophil caspase1 activity, reversible by  
600 an IFN-I receptor (IFNAR) blocking antibody. Transcriptional analysis revealed a robust IFN-  
601 I signature and elevated expression of inflammasome genes encoding for caspase1 and IL-1 $\beta$   
602 in neutrophils of infected mice, which were also inhibited by blocking IFNAR signaling,  
603 suggesting that IFN-I may also prime for inflammasome activation in mice. Notably, the anti-  
604 IFNAR treatment did not affect neutrophil recruitment or NETosis, which is consistent with  
605 another COVID-19 model using transgenic human ACE2, where IFNAR knockout inhibited  
606 recruitment of monocytes and lymphocytes, but not neutrophils, to infected lungs <sup>50</sup>.

607 Inflammasomes were initially studied in macrophages, revealing a plethora of molecular  
608 mechanisms regulating inflammasome assembly <sup>51</sup>. Macrophage inflammasome activation has  
609 emerged as a major factor also in COVID-19 <sup>17</sup>. Interestingly, macrophage inflammasome  
610 activation was recognized to be IFN-I mediated in an experimental rhesus macaque COVID-  
611 19 model <sup>52</sup>. However, due to the abundance of neutrophils compared with cells of  
612 monocyte/macrophage lineage <sup>53,54</sup>, the significance of neutrophil inflammasomes in COVID-  
613 19 is likely underestimated. Our results highlight inflammasomes as an additional important  
614 inflammatory mechanism in neutrophils <sup>14</sup>, complementing their role in phagocytosis, reactive  
615 oxygen species generation, degranulation, and NETosis <sup>32</sup>.

616 SARS-CoV-2 can directly activate inflammasomes in cells of the monocyte/macrophage  
617 lineage <sup>17</sup>. Our study investigated whether SARS-CoV-2 can provide the first or second signal  
618 for inflammasome activation in neutrophils. However, we found no evidence of direct virus-  
619 induced inflammasome activation in neutrophils. The difference between macrophages and

620 neutrophils in their susceptibility to SARS-CoV-2 could depend on many factors. Both cell  
621 types express ACE2, the receptor for SARS-CoV-2, but may differ in ACE2 expression levels  
622 <sup>55</sup>. Furthermore, the intracellular environment of macrophages is better suited for viral  
623 replication <sup>56</sup>, while neutrophils focus on phagocytosis and antimicrobial responses <sup>32,57</sup>.  
624 Additionally, pathogen opsonization can trigger inflammasomes in macrophages <sup>58</sup> but is not a  
625 primary function of neutrophils. Therefore, our findings suggest neutrophil inflammasome  
626 activation in response to SARS-CoV-2 likely results from interactions with infected and/or  
627 dying cells in the lungs, rather than direct virus activation. To note, whether SARS-CoV-2 can  
628 induce neutrophil inflammasomes through immune complex-mediated mechanisms, as seen in  
629 monocytes/macrophages <sup>17</sup> remains to be determined.

630 In this study, we demonstrated IFN-I as the first signal for NLRP3 inflammasome activation in  
631 neutrophils. While prior research has explored IFN-inflammasome crosstalk <sup>59</sup>, priming  
632 capacity of IFN-I remained unclear. While IFN-I promotes inflammasomes in epithelial cells  
633 <sup>60</sup> it can also dampen IL-1 $\beta$  in macrophages <sup>61</sup>. Plausibly, initial IFN-I exposure may upregulate  
634 inflammasome genes, whereas prolonged activity could hinder IFN-I signaling via “negative  
635 feedback” loop, in line with our findings of inflammasome exhaustion in circulating  
636 neutrophils of severe COVID-19 patients.

637 Our study also unveiled distinct gene profiles in LDGs and PMNs from severe COVID-19  
638 patients. LDGs exhibited upregulation of genes related to DNA replication and cell cycle,  
639 indicating immaturity, and confirming our prior findings <sup>7</sup>. Conversely, PMNs displayed  
640 heightened NLR signaling, suggesting a robust response to pathogens. While our study  
641 compared PMNs and LDGs, and the COVID-19 Immune Atlas single cell analysis represented  
642 a broader classification of mature and immature neutrophils, the alignment of our results with  
643 the atlas provides further support for the distinct characteristics of these two neutrophil



644 populations in severe COVID-19. Notably, IL-18 gene expression and secretion after *ex vivo*  
645 stimulation were higher in LDGs than PMNs. To note, PMN's lack of IL-18 secretion is not  
646 due to lack of protein, as they constitutively express significant amounts intracellularly<sup>62</sup>. This  
647 indicates a similarity between LDGs and monocytes/macrophages in inflammasome mediated  
648 IL-18 processing, possibly lost during neutrophil maturation.

649

650 The present study has some limitations worth discussing. Firstly, the relatively small human  
651 sample size may limit the generalizability of the findings. While RNA-seq provided valuable  
652 insights into gene expression profiles of PMNs and LDGs, we did not perform functional  
653 validation of the identified pathways in this study. Regarding our experimental SARS-CoV-2  
654 infected model, the high virus input might trigger robust immune responses that differ from  
655 typical human infections, and the short-lived virus replication in the applied model does not  
656 capture the effect of prolonged antigen exposure or the complex inflammatory milieu seen in  
657 human cases. The prominent role of neutrophils in the immune response to viral infections is  
658 widely recognized<sup>44,45</sup> and it would be valuable to compare these findings to neutrophil  
659 responses in other viral respiratory infections.

660

661 Taken together, our findings provide valuable insights into neutrophil involvement in COVID-  
662 19 and possibly other viral respiratory infections. However, further research is needed to fully  
663 grasp the role of neutrophil inflammasomes in COVID-19 pathogenesis. This increased  
664 understanding may facilitate the development of targeted treatment approaches for COVID-19.  
665 The next steps involve validating the pathways and genes identified as potential therapeutic  
666 targets and assessing their COVID-19 specificity. Prospectively, these strategies could be  
667 extended to address upcoming respiratory virus pandemics, where neutrophils and  
668 inflammasomes provide major pathogenic contributions.

## 669 **Contributors**

670 L.E.C.: conceptualization, data curation, formal analysis, investigation, software, validation,  
671 visualization, writing– original draft; S.T.J.: investigation, writing – review & editing; Sa.M.:  
672 investigation; Si.M.: investigation; R.K.: resources; L.K.; investigation, writing – review &  
673 editing; Ta.S.: resources; J-P.P.: resources; Anu.K.: funding acquisition, resources, writing –  
674 review & editing; E.K.: supervision, writing – review & editing; H.L.: resources; P.M.:  
675 resources, writing – review & editing; Anj.K.: investigation, methodology, supervision,  
676 validation, visualization, writing – review & editing; O.V.: funding acquisition, resources;  
677 To.S.: conceptualization, data curation, formal analysis, funding acquisition, investigation,  
678 methodology, project administration, supervision, validation, writing – original draft.

679

## 680 **Declaration of Competing Interest**

681 All authors declare no financial competing interests related to the study.

682

## 683 **Acknowledgements**

684

685 This work was financed by grants by the Academy of Finland to To.S. (321809), Anu.K.  
686 (336439 and 335527); grants by the Helsinki University Hospital funds to O.V. (TYH  
687 2021343); EU Horizon 2020 programme VEO (874735) to O.V.; Finnish governmental  
688 subsidy for Health Science Research (TYH 2021315) to Anu.K.; Paulon Säätiö to L.E.C.;  
689 Suomen Lääketieteen Säätiö to L.E.C.; Jane and Aatos Erkko foundation to O.V. The funders  
690 had no role in study design, data collection and analysis, nor decision to publish, or preparation  
691 of the manuscript.

692

693 RNA isolation, library preparations and RNA sequencing was performed at the Institute for  
694 Molecular Medicine Finland FIMM, Genomics unit supported by HiLIFE and Biocenter  
695 Finland. The authors also thank M. Utriainen for expert technical assistance.

696

## References

697

- 698 1 Wilk AJ, Lee MJ, Wei B, *et al.* Multi-omic profiling reveals widespread  
699 dysregulation of innate immunity and hematopoiesis in COVID-19. *Journal of*  
700 *Experimental Medicine* 2021; **218**. DOI:10.1084/jem.20210582.
- 701 2 Blanco-Melo D, Nilsson-Payant BE, Liu WC, *et al.* Imbalanced Host Response  
702 to SARS-CoV-2 Drives Development of COVID-19. *Cell* 2020; **181**: 1036-  
703 1045.e9.
- 704 3 Hadjadj J, Yatim N, Barnabei L, *et al.* Impaired type I interferon activity and  
705 inflammatory responses in severe COVID-19 patients. .
- 706 4 Domizio J Di, Gulen MF, Saidoune F, *et al.* The cGAS–STING pathway drives  
707 type I IFN immunopathology in COVID-19. *Nature* 2022; **603**: 145–51.
- 708 5 Barnes BJ, Adrover JM, Baxter-Stoltzfus A, *et al.* Targeting potential drivers of  
709 COVID-19: Neutrophil extracellular traps. *Journal of Experimental Medicine*.  
710 2020; **217**. DOI:10.1084/jem.20200652.
- 711 6 Radermecker C, Detrembleur N, Guiot J, *et al.* Neutrophil extracellular traps  
712 infiltrate the lung airway, interstitial, and vascular compartments in severe  
713 COVID-19. *Journal of Experimental Medicine* 2020; **217**.  
714 DOI:10.1084/jem.20201012.
- 715 7 Cabrera LE, Pekkarinen PT, Alander M, *et al.* Characterization of low-density  
716 granulocytes in COVID-19. *PLoS Pathog* 2021; **17**.  
717 DOI:10.1371/journal.ppat.1009721.
- 718 8 LaSalle TJ, Gonye ALK, Freeman SS, *et al.* Longitudinal characterization of  
719 circulating neutrophils uncovers phenotypes associated with severity in  
720 hospitalized COVID-19 patients. *Cell Rep Med* 2022; **3**.  
721 DOI:10.1016/j.xcrm.2022.100779.
- 722 9 Schulte-Schrepping J, Reusch N, Paclik D, *et al.* Severe COVID-19 Is Marked  
723 by a Dysregulated Myeloid Cell Compartment. *Cell* 2020; **182**: 1419-1440.e23.
- 724 10 Ueda Y, Kondo M, Kelsoe G. Inflammation and the reciprocal production of  
725 granulocytes and lymphocytes in bone marrow. *Journal of Experimental*  
726 *Medicine* 2005; **201**: 1771–80.
- 727 11 Zuo Y, Yalavarthi S, Shi H, *et al.* Neutrophil extracellular traps in COVID-19.  
728 *JCI Insight* 2020; **5**. DOI:10.1172/jci.insight.138999.
- 729 12 Potere N, Giuseppe M, Buono D, *et al.* Interleukin-1 and the NLRP3  
730 inflammasome in COVID-19: Pathogenetic and therapeutic implications. 2022.  
731 DOI:10.1016/j.
- 732 13 Lechtenberg BC, Mace PD, Riedl SJ. Structural mechanisms in NLR  
733 inflammasome signaling. *Curr Opin Struct Biol.* 2014; **29**: 17–25.
- 734 14 Aymonnier K, Ng J, Fredenburgh LE, *et al.* Inflammasome activation in  
735 neutrophils of patients with severe COVID-19. *Blood Adv* 2022; **6**: 2001–13.
- 736 15 Courjon J, Dufies O, Robert A, *et al.* Heterogeneous NLRP3 inflammasome  
737 signature in circulating myeloid cells as a biomarker of COVID-19 severity.  
738 *Blood Adv* 2021; **5**: 1523–34.
- 739 16 Leal VNC, Andrade MMS, Teixeira FME, *et al.* Severe COVID-19 patients  
740 show a dysregulation of the NLRP3 inflammasome in circulating neutrophils.  
741 *Scand J Immunol* 2022. DOI:10.1111/sji.13247.
- 742 17 Sefik E, Qu R, Junqueira C, *et al.* Inflammasome activation in infected  
743 macrophages drives COVID-19 pathology. *Nature* 2022; **606**: 585–93.

- 744 18 Gawish R, Starkl P, Pimenov L, *et al.* ACE2 is the critical in vivo receptor for  
745 SARS-CoV-2 in a novel COVID-19 mouse model with TNF-and IFN $\gamma$ -driven  
746 immunopathology. *Elife* 2022; **11**. DOI:10.7554/eLife.74623.
- 747 19 Rusanen J, Kareinen L, Szirovicza L, *et al.* A Generic, Scalable, and Rapid  
748 Time-Resolved Förster Resonance Energy Transfer-Based Assay for Antigen  
749 Detection-SARS-CoV-2 as a Proof of Concept. 2021. DOI:10.1128/mBio.
- 750 20 Kallio MA, Tuimala JT, Hupponen T, *et al.* Chipster: User-friendly analysis  
751 software for microarray and other high-throughput data. *BMC Genomics* 2011;  
752 **12**. DOI:10.1186/1471-2164-12-507.
- 753 21 Liu P, Ewald J, Pang Z, *et al.* ExpressAnalyst: A unified platform for RNA-  
754 sequencing analysis in non-model species. *Nat Commun* 2023; **14**: 2995.
- 755 22 Emig D, Salomonis N, Baumbach J, Lengauer T, Conklin BR, Albrecht M.  
756 AltAnalyze and DomainGraph: Analyzing and visualizing exon expression data.  
757 *Nucleic Acids Res* 2010; **38**. DOI:10.1093/nar/gkq405.
- 758 23 Babicki S, Arndt D, Marcu A, *et al.* Heatmapper: web-enabled heat mapping for  
759 all. *Nucleic Acids Res* 2016; **44**: W147–53.
- 760 24 Steen CB, Liu CL, Alizadeh AA, Newman AM. Profiling cell type abundance  
761 and expression in bulk tissues with CIBERSORTx. In: *Methods in Molecular*  
762 *Biology*. Humana Press Inc., 2020: 135–57.
- 763 25 Li Y, He Y, Liang Z, *et al.* Alterations of specific chromatin conformation  
764 affect ATRA-induced leukemia cell differentiation. *Cell Death Dis* 2018; **9**.  
765 DOI:10.1038/s41419-017-0173-6.
- 766 26 CZ CELLxGENE Discover. Chan Zuckerberg Initiative.  
767 <https://cellxgene.cziscience.com/>.
- 768 27 Corman VM, Landt O, Kaiser M, *et al.* Detection of 2019 novel coronavirus  
769 (2019-nCoV) by real-time RT-PCR. *Eurosurveillance* 2020; **25**.  
770 DOI:10.2807/1560-7917.ES.2020.25.3.2000045.
- 771 28 Dagotto G, Mercado NB, Martinez DR, *et al.* Comparison of Subgenomic and  
772 Total RNA in SARS-CoV-2-Challenged Rhesus Macaques. 2021.  
773 DOI:10.1128/JVI.
- 774 29 Kant R, Kareinen L, Smura T, *et al.* Common laboratory mice are susceptible to  
775 infection with the SARS-CoV-2 beta variant. *Viruses* 2021; **13**.  
776 DOI:10.3390/v13112263.
- 777 30 Schmid AS, Hemmerle T, Pretto F, Kipar A, Neri D. Antibody-based targeted  
778 delivery of interleukin-4 synergizes with dexamethasone for the reduction of  
779 inflammation in arthritis. *Rheumatology (United Kingdom)* 2018; **57**: 748–55.
- 780 31 Seehusen F, Clark JJ, Sharma P, *et al.* Neuroinvasion and Neurotropism by  
781 SARS-CoV-2 Variants in the K18-hACE2 Mouse. *Viruses* 2022; **14**.  
782 DOI:10.3390/v14051020.
- 783 32 Rosales C. Neutrophil: A cell with many roles in inflammation or several cell  
784 types? *Front Physiol.* 2018; **9**. DOI:10.3389/fphys.2018.00113.
- 785 33 Walle L Vande, Lamkanfi M. Inflammasomes: Caspase-1-activating platforms  
786 with critical roles in host defense. *Front Microbiol* 2011; **2**.  
787 DOI:10.3389/fmicb.2011.00003.
- 788 34 Perregaux D, Gabel CA. Interleukin-1 $\beta$  maturation and release in response to  
789 ATP and nigericin. Evidence that potassium depletion mediated by these agents  
790 is a necessary and common feature of their activity. *Journal of Biological*  
791 *Chemistry* 1994; **269**: 15195–203.

- 792 35 Gong YN, Wang X, Wang J, *et al.* Chemical probing reveals insights into the  
793 signaling mechanism of inflammasome activation. *Cell Res* 2010; **20**: 1289–  
794 305.
- 795 36 Grigorieva D V., Gorudko I V., Sokolov A V., *et al.* Myeloperoxidase  
796 stimulates neutrophil degranulation. *Bull Exp Biol Med* 2016; **161**: 495–500.
- 797 37 Silvin A, Chapuis N, Dunsmore G, *et al.* Elevated Calprotectin and Abnormal  
798 Myeloid Cell Subsets Discriminate Severe from Mild COVID-19. *Cell* 2020;  
799 **182**: 1401-1418.e18.
- 800 38 Simard JC, Cesaro A, Chapeton-Montes J, *et al.* S100A8 and S100A9 induce  
801 cytokine expression and regulate the NLRP3 inflammasome via ROS-dependent  
802 activation of NF- $\kappa$ B(1.). *PLoS One* 2013; **8**.  
803 DOI:10.1371/journal.pone.0072138.
- 804 39 Jacob C, Leport M, Szilagyi C, Allen JM, Bertrand C, Lagente V. DMSO-  
805 treated HL60 cells: a model of neutrophil-like cells mainly expressing PDE4B  
806 subtype. [www.elsevier.com/locate/intimp](http://www.elsevier.com/locate/intimp).
- 807 40 Tang Y, Xu Q, Luo H, *et al.* Excessive IL-10 and IL-18 trigger hemophagocytic  
808 lymphohistiocytosis-like hyperinflammation and enhanced myelopoiesis.  
809 *Journal of Allergy and Clinical Immunology* 2022; **150**: 1154–67.
- 810 41 Xue Y, Yang D, Vogel P, *et al.* Cardiopulmonary Injury in the Syrian Hamster  
811 Model of COVID-19. *Viruses* 2022; **14**. DOI:10.3390/v14071403.
- 812 42 Vargas F, Castanheira S, Nguyen R, *et al.* Intravital imaging of 3 different  
813 microvascular beds in SARS-CoV-2-infected mice.  
814 DOI:10.1182/bloodadvances.2022009430/2057344/bloodadvances.2022009430.  
815 pdf.
- 816 43 Winkler ES, Bailey AL, Kafai NM, *et al.* SARS-CoV-2 infection of human  
817 ACE2-transgenic mice causes severe lung inflammation and impaired function.  
818 *Nat Immunol* 2020; **21**: 1327–35.
- 819 44 Zhang Y, Wang Q, Mackay CR, Ng LG, Kwok I. Neutrophil subsets and their  
820 differential roles in viral respiratory diseases. *J Leukoc Biol.* 2022; **111**: 1159–  
821 73.
- 822 45 Camp J V., Jonsson CB. A role for neutrophils in viral respiratory disease. *Front*  
823 *Immunol.* 2017; **8**. DOI:10.3389/fimmu.2017.00550.
- 824 46 McKenna E, Wubben R, Isaza-Correa JM, *et al.* Neutrophils in COVID-19: Not  
825 Innocent Bystanders. *Front Immunol.* 2022; **13**.  
826 DOI:10.3389/fimmu.2022.864387.
- 827 47 Lee JS, Park S, Jeong HW, *et al.* Immunophenotyping of covid-19 and influenza  
828 highlights the role of type i interferons in development of severe covid-19. *Sci*  
829 *Immunol* 2020; **5**. DOI:10.1126/sciimmunol.abd1554.
- 830 48 Sinha S, Rosin NL, Arora R, *et al.* Dexamethasone modulates immature  
831 neutrophils and interferon programming in severe COVID-19. *Nat Med* 2022;  
832 **28**: 201–11.
- 833 49 Takeuchi O, Akira S. Pattern Recognition Receptors and Inflammation. *Cell.*  
834 2010; **140**: 805–20.
- 835 50 Israelow B, Song E, Mao T, *et al.* Mouse model of SARS-CoV-2 reveals  
836 inflammatory role of type i interferon signaling. *Journal of Experimental*  
837 *Medicine* 2020; **217**. DOI:10.1084/JEM.20201241.
- 838 51 Broz P, Dixit VM. Inflammasomes: Mechanism of assembly, regulation and  
839 signalling. *Nat Rev Immunol.* 2016; **16**: 407–20.



- 840 52 Hoang TN, Viox EG, Upadhyay AA, *et al.* Modulation of type I interferon  
841 responses potently inhibits SARS-CoV-2 replication and inflammation in rhesus  
842 macaques. DOI:10.1101/2022.10.21.512606.
- 843 53 Lucas C, Wong P, Klein J, *et al.* Longitudinal analyses reveal immunological  
844 misfiring in severe COVID-19. *Nature* 2020; **584**: 463–9.
- 845 54 Huang C, Wang Y, Li X, *et al.* Clinical features of patients infected with 2019  
846 novel coronavirus in Wuhan, China. *The Lancet* 2020; **395**: 497–506.
- 847 55 Song X, Hu W, Yu H, *et al.* Little to no expression of angiotensin-converting  
848 enzyme-2 on most human peripheral blood immune cells but highly expressed  
849 on tissue macrophages. *Cytometry Part A* 2020; published online Feb 1.  
850 DOI:10.1002/cyto.a.24285.
- 851 56 Nikitina E, Larionova I, Choinzonov E, Kzhyshkowska J. Monocytes and  
852 macrophages as viral targets and reservoirs. *Int J Mol Sci.* 2018; **19**.  
853 DOI:10.3390/ijms19092821.
- 854 57 Patel AA, Ginhoux F, Yona S. Monocytes, macrophages, dendritic cells and  
855 neutrophils: an update on lifespan kinetics in health and disease. *Immunology.*  
856 2021; **163**: 250–61.
- 857 58 Zhou J, Ludlow LE, Hasang W, Rogerson SJ, Jaworowski A. Opsonization of  
858 malaria-infected erythrocytes activates the inflammasome and enhances  
859 inflammatory cytokine secretion by human macrophages. *Malar J* 2012; **11**.  
860 DOI:10.1186/1475-2875-11-343.
- 861 59 Labzin LI, Lauterbach MAR, Latz E. Interferons and inflammasomes:  
862 Cooperation and counterregulation in disease. *Journal of Allergy and Clinical*  
863 *Immunology.* 2016; **138**: 37–46.
- 864 60 Pothlichet J, Meunier I, Davis BK, *et al.* Type I IFN Triggers RIG-  
865 I/TLR3/NLRP3-dependent Inflammasome Activation in Influenza A Virus  
866 Infected Cells. *PLoS Pathog* 2013; **9**. DOI:10.1371/journal.ppat.1003256.
- 867 61 Kopitar-Jerala N. The role of interferons in inflammation and inflammasome  
868 activation. *Front Immunol.* 2017; **8**. DOI:10.3389/fimmu.2017.00873.
- 869 62 Robertson SE, Young JD, Kitson S, *et al.* Expression and alternative processing  
870 of IL-18 in human neutrophils. *Eur J Immunol* 2006; **36**: 722–31.
- 871 63 Rubio-Rivas M, Mora-Luján JM, Formiga F, *et al.* WHO Ordinal Scale and  
872 Inflammation Risk Categories in COVID-19. Comparative Study of the Severity  
873 Scales. *J Gen Intern Med* 2022; **37**: 1980–7.  
874  
875

876

## Figure legends

877

878

879

880

881

882

883

884

885

886

887

888

**Figure 1. Comparison of gene expression in granulocyte populations of COVID-19 patients using RNA-seq analysis.** (A) Principal component analysis (PCA) of the RNA-seq samples (n = 7 for HC PMNs, n = 19 for COVID-19 PMNs (n = 11 and 8 for severe and mild, respectively), n = 6 for severe COVID-19 LDGs). (B) Ridgeline diagrams depicting the top 10 enriched signal pathways from the genes differentially expressed by LDGs versus PMNs during severe COVID-19, including an overrepresentation analysis (ORA) using KEGG database and gene-set enrichment analysis (GSEA) according to Reactome database. Both enrichment analyses were made using ExpressAnalyst and are sorted by P-value, obtained from Welch's t-test. (C) Heatmap of the top 95 differentially expressed genes between PMNs from healthy controls, mild and severe COVID-19, as well as LDGs from severe disease, identified by unsupervised ICGS analysis based on correlation, using AltAnalyze software.



889 **Figure 2. Increased IFN-I related gene expression in mature COVID-19 neutrophils.**

890 (A) Deconvoluted RNA-seq data. The cellular composition in isolated PMN and LDG fractions was  
891 estimated using CIBERSORTx through the identification of cell populations based on RNA-seq. The bar  
892 plots in the figure represent the cell composition of each RNA-seq sample, offering insights on sample  
893 purity.

894 (B) Heatmap of differentially expressed IFN-related genes in COVID-19 PMNs and LDGs as compared  
895 to HC PMNs. RNA sequencing was performed on purified PMNs from healthy controls, mild COVID-19  
896 and severe COVID-19, as well as severe COVID-19 LDGs. The heatmap was reduced to include only the  
897 samples with the highest purity for their cell type, determined by a cell fraction over 0.8 of mature or  
898 immature neutrophils for PMNs and LDGs, respectively, as identified by CIBERSORTx. The heatmap  
899 was clustered by complete linkage and ordered by Spearman's rank. n = 13 COVID-19 PMNs (7 severe,  
900 6 mild), n = 4 severe COVID-19 LDGs and n = 5 HC PMNs.

901

902 **Figure 3. Inflammasome related gene expression and cytokine secretion in PMNs during severe**  
903 **COVID-19. (A-B)** Ridgeline diagrams of overrepresentation analyses (ORA) according to Reactome and  
904 KEGG databases, depicting the top 10 enriched signaling pathways in PMNs during severe COVID-19  
905 compared to (A) healthy controls and (B) mild COVID-19. (C) IL-1 $\beta$  and (D) IL-18 levels in 24-h cell  
906 culture supernatants from COVID-19 (n = 11 for IL-1 $\beta$  and 9 for IL-18) and HC PMNs (n =6 for both).  
907 (E) IL-1 $\beta$  and (F) IL-18 levels in 24-h cell culture supernatant from PMNs exposed or non-exposed to  
908 purified SARS-CoV-2 viral particles (10 virus particles / PMN) (n = 3). (G) Caspase1 activity in PMNs  
909 following a 2-h stimulation with nigericin or purified SARS-CoV-2 viral particles (10 virus particles /  
910 PMN). For HC PMNs, n = 9 for mock and nigericin and n = 6 for SARS-CoV-2 exposure. For COVID-  
911 19 PMNs, n = 12 for mock and nigericin and n = 9 for SARS-CoV-2 exposure. \*p < 0.05 and \*\*p < 0.01.  
912 Data presented as mean  $\pm$  SD. Tukey's multiple comparisons test for mixed-effect analysis was applied  
913 for (G), meanwhile P values for (C-F) were calculated with the Mann-Whitney U-test.  
914

915 **Figure 4. Comparative neutrophil transcriptomics of COVID-19 and non-COVID-19 patients.**  
916 Bar graphs represent the activation levels of selected pathways and processes as identified by neutrophil  
917 transcriptomics. The analysis includes IFN- $\alpha$  responses, IL-1 $\beta$  production, TLR signaling, NLRP3  
918 inflammasomes, and pyroptosis as determined through the Gene Ontology (GO) database. The NOD-like  
919 receptor signaling pathway was investigated using the Kyoto Encyclopedia of Genes and Genomes  
920 (KEGG) database, and the inflammasome pathway was explored via the REACTOME database. The  
921 graphs compare the activation levels of these pathways in healthy controls (HC), non-COVID patients  
922 with similar symptoms (COVID-19 negative), and COVID-19 positive individuals. Statistical significance  
923 is denoted as follows: \* $p < 0.05$ , \*\* $p < 0.01$ , \*\*\* $p < 0.001$ , \*\*\*\* $p < 0.0001$ . P values were calculated with  
924 Kruskal-Wallis test.  
925

926 **Figure 5. IFN-I primes inflammasome activation while COVID-19 PMNs show defective**  
927 **inflammasome responses *ex vivo*.** Isolated HC or COVID-19 PMNs were non-stimulated or stimulated  
928 4h with IFN-I (combination of  $2.7 \times 10^4$  IU/ml IFN- $\alpha$  and IFN- $\beta$ ) or 20 ng/ml LPS (1<sup>st</sup> signal), followed by  
929 4h with 2.5  $\mu$ M nigericin or purified SARS-CoV-2 (10:1 virus/PMNs) (2<sup>nd</sup> signal). Then, (A) western blot  
930 of pro-IL-1 $\beta$  (31 kD) and active IL-1 $\beta$  (17 kD) was performed from HC PMNs supernatant and cell  
931 lysates, (B) IL-1 $\beta$  (n = 5 HC PMN and 9 COVID-19 PMN) and (C) MPO (n= 5 HC PMN and 9 COVID-  
932 19 PMN) were measured from supernatants by ELISA. (D-E) Effect of inflammasome inhibitor MCC950  
933 (2  $\mu$ g/ml, added simultaneously with nigericin) on IL-1 $\beta$  secretion in HC (D) and severe COVID-19 PMN  
934 (E) supernatant (n = 3). (F) LDH and (G) IL-8 in HC and severe COVID-19 PMN supernatants (n = 3).  
935 (H-K) RT-qPCR of selected mRNAs in IFN-I or LPS-primed HC and COVID-19 PMNs (n = 6-8 HC  
936 PMN and 7-10 COVID-19 PMN). \*p < 0.05, \*\*p < 0.01, \*\*\*p < 0.001, \*\*\*\*p < 0.0001; n = 2-4. Data  
937 were presented as mean  $\pm$  SD. P values calculated with Kruskal-Wallis test for the comparison between  
938 treatments by group (HC or COVID-19 PMNs), and Mann-Whitney test for the comparison between HC  
939 and COVID-19 PMNs by individual treatment for (B-G), and Two-way ANOVA Tukey's multiple  
940 comparisons test for (B, H-K). Data presented as mean  $\pm$  SD.  
941

942 **Figure 6. Correlation analysis between clinical parameters and *ex vivo* PMN inflammasome**  
943 **activation. (A)** Spearman's correlation matrix depicting the relationships among clinical parameters and  
944 results of *ex vivo* experimentation. For the WHO ordinal scale, the baseline parameters were used. **(B-C)**  
945 Linear regression analysis demonstrating the associations between: **(B)** Positive association between PMN  
946 Caspase1 activity, measured after *ex vivo* nigericin stimulation, and the levels of Calprotectin in the  
947 matched patient's peripheral blood; **(C)** Negative association between *ex vivo* stimulated PMN IL-1 $\beta$   
948 levels (LPS+Nig) and the blood neutrophil count in matched patients at the time of sampling (n=12).  
949 *LOS* = length of stay. *WHO* = World Health Organization. *Min* = minimum. *Casp1* = caspase1. *LPS* or  
950 *IFN + nig* = lipopolysaccharide or type I interferon + nigericin *ex vivo* stimulation.  
951

952 **Figure 7. Immature neutrophils express IL-18 in response to inflammasome activation.**  
953 (A) Heatmap depicting selected differentially expressed inflammasome related genes from RNA  
954 sequencing performed in PMNs from HC, mild and severe COVID-19, as well as severe COVID-19  
955 LDGs. Only the samples with the highest purity, determined by a cell fraction over 0.8 of mature or  
956 immature neutrophils for PMN and LDG, respectively, (identified by CIBERSORTx) are included. The  
957 heatmap was clustered by complete linkage and ordered by Spearman's rank.  
958 (B) UMAP analysis of the COVID-19 Immune Atlas, which integrates 5 public COVID-19 PBMC single-  
959 cell transcriptomics datasets, created using CELLxGENE. (Top) UMAP showing the clustering of CD16<sup>+</sup>  
960 cells (mature, FCGR3B expressing cells) and CD66b<sup>+</sup> cells (immature, CEACAM8 expressing cells).  
961 Each dot represents a single cell colored according to the expression level of a selected gene. The color  
962 scale ranges from green (low expression) to purple (high expression). (Bottom) Pie chart summarizing the  
963 percentage of mature (black) and immature (blue) cells in the dataset.  
964 (C) The fraction of mature and immature neutrophils cells expressing inflammasome related genes  
965 identified in Figure 7B are shown in a bar graph. For each gene, the proportion of expressing cells is  
966 shown in light blue, while the proportion of negative or not-expressing cells is shown in gray. Zoomed-in  
967 bar graph depicts the proportion of mature and immature cells expressing each gene.  
968 (D-G) Isolated COVID-19 LDGs or HL-60 cells (differentiated for 5 days with 1% DMSO) were non-  
969 stimulated or stimulated 4h with IFN-I or LPS (1<sup>st</sup> signal), followed by 4h with nigericin (2<sup>nd</sup> signal) in  
970 the presence or absence of inflammasome inhibitors MCC950 or YVAD as previously. Secretion of (D,  
971 F) IL-1 $\beta$  and (E, G) IL-18 were measured from the supernatants by ELISA (n = 2 for LDGs and 3-5 for  
972 HL-60).  
973 \*p < 0.05 and \*\*p < 0.01. P values calculated with Kruskal-Wallis test. Data presented as mean  $\pm$  SD.  
974 (H) Volcano plot of differentiated vs undifferentiated HL-60 cells gene expression from GSE93996, with  
975 inflammasome related genes marked in blue. Only significant DE genes are shown (adjusted p value <  
976 0.05).

977 **Figure 8. Neutrophil accumulation in the lungs correlates with viral loads in SARS-CoV-2 infected**  
978 **mice.** Female BALB/c mice were intranasally inoculated with  $5 \times 10^5$  TCID50 SARS-CoV-2 MaVie strain  
979 or PBS as control and euthanized at 2 dpi or 4 dpi.  
980 (A) RNA was isolated from lungs and subjected to RT-qPCR targeting viral subE and GAPDH as  
981 housekeeping gene. The relative expression of subE was measured using the comparative Ct method as  
982 compared to mock-infected control (in which subE was undetectable but set to 40 Ct) \*\*\*\* p < 0.0001. P  
983 values calculated with Welch's t-test.  
984 (B) Quantification based on morphometric analysis that determines the area of immunolabelling for  
985 SARS-CoV-2 nucleoprotein in relation to total tissue area. \*\*\*p < 0.001. P values calculated with Welch's  
986 t-test.  
987 (C) Quantification of Ly-6G based on morphometric analysis that determines the area of immunolabelling  
988 for Ly6G in relation to total tissue area in mock-infected controls. \*\*\*\* p < 0.0001. P values calculated  
989 with ordinary one-way ANOVA using Tukey's multiple comparisons test. Black line represents the mean.  
990 (D) Left column: immunohistochemistry for SARS-CoV-2 nucleoprotein; right column:  
991 immunohistochemistry for Ly6G (neutrophil marker), hematoxylin counterstain. Bars = 500  $\mu$ m (large  
992 images) and 50  $\mu$ m (insets).  
993 At 2 dpi (top), the arrow points at a bronchus with viral antigen expression in epithelial cells. A close-up  
994 of the bronchus (bottom; B: bronchial lumen) shows degenerated and slough off antigen positive epithelial  
995 cells. Adjacent alveoli exhibit viral antigen expression in typeI (arrowhead) and typeII (arrow)  
996 pneumocytes. The overview (top) shows neutrophils between the infected bronchial (arrow) epithelial  
997 cells, in parenchymal areas (arrowhead; right inset) and in capillaries (arrowheads). A close-up of the  
998 bronchus (bottom; B: bronchial lumen) highlights numerous neutrophils between degenerate (arrowheads)  
999 epithelial cells.  
1000 At 4 dpi (middle), there are focal areas with antigen expression in alveolar epithelial cells and infiltrating  
1001 macrophages. Neutrophils are present among the infiltrating cells (arrow) as individual cells (inset:  
1002 arrows) or in aggregates (inset: arrowhead).  
1003 The bottom shows the lung of a mock-infected control animal. There is no viral antigen expression.  
1004 Staining for Ly6G depicts individual neutrophils in larger vessels (inset: arrow) or in capillaries (inset:  
1005 arrowheads).  
1006  
1007  
1008

1009 **Figure 9. Neutrophils of SARS-CoV-2 infected mice display increased caspase1 activation ability**  
1010 **that is dependent on IFN-I.**

1011 Female BALB/c mice were intranasally inoculated with  $5 \times 10^5$  TCID50 SARS-CoV-2 MaVie strain or  
1012 PBS as control. Lungs were harvested at 2 and 4 dpi and Ly-6G+ neutrophils isolated based on positive  
1013 selection with magnetic beads. RNA was isolated and subjected to transcriptomic analysis by RNA-seq.  
1014 (A) Principal component analysis (PCA) of the PBS-inoculated control and SARS-CoV-2 infected mice  
1015 lung neutrophil RNA-seq samples. (B) Heatmap of the top DEGs. (C) Volcano plots of DEGs between  
1016 neutrophils isolated from SARS-CoV-2 infected mice versus uninfected PBS-inoculated mice. Blue points  
1017 represent significant terms (adjusted p-value < 0.05), while smaller gray points represent non-significant  
1018 terms. Relevant inflammasome and interferon related genes are shown with larger and darker blue points.  
1019 (D) Caspase1 activity in isolated mice neutrophils following a 2-h stimulation with nigericin was  
1020 assessed by a bioluminescence method (Caspase-Glo® 1 Inflammasome Assay).

1021 (E-G) Mice were intraperitoneally inoculated with 250 µg anti-IFNAR or IgG1 isotype control directly  
1022 after infection with SARS-CoV-2 and lung neutrophils isolated at 2 dpi (including also intranasally PBS-  
1023 inoculated control mice without intraperitoneal injection).

1024 (E) Caspase1 activity was assessed following a 2-h stimulation with nigericin by bioluminescence  
1025 method.

1026 (F-G) RNA was isolated from isolated neutrophils and fold change mRNA expressions of (C) Caspase1  
1027 (Casp1) and (D) IL-1β (IL1b) in isotype control and anti-IFNAR treated infected mice as compared to  
1028 mock-infected control mice assessed by RT-qPCR.

1029 DEG = differentially expressed genes.

1030 \*p < 0.05, and \*\*p < 0.01. P values for D, E and H panels were calculated with ordinary one-way  
1031 ANOVA using Tukey's multiple comparisons. Welch's t-test was used for panels F and G. Data  
1032 presented as mean ± SD.



1033 **Supplementary figure legends**

1034

1035

1036

**Supplementary Figure 1. Enriched pathways and differentially expressed genes in severe COVID-19 PMNs and LDGs.**

1037

1038

1039

1040

1041

(A-B) Volcano plots of enriched gene sets in severe COVID-19 PMNs versus (A) HC PMNs and (B) severe COVID-19 LDGs, using KEGG database. Each point represents a single gene set, where the x-axis measures its odds ratio, while the y-axis shows its  $-\log(p\text{-value})$ . Blue points represent significant terms (adjusted p-value < 0.05), where darker points represent more significant terms, while smaller gray points represent non-significant terms.

1042

1043

1044

1045

1046

1047

1048

(C-D) Volcano plots of DEGs between severe COVID-19 PMNs versus (C) HC PMNs and (D) severe COVID-19 LDGs. Blue points represent significant terms (adjusted p-value < 0.05), while smaller gray points represent non-significant terms. Relevant inflammasome related or -predicted genes based on the literature, according to GENESHOT (34), are shown with a larger and darker blue point.

1049

1050

1051

1052

1053

(E-F) Pie charts of interferon and inflammasome related genes, according to GENESHOT from the identified DEGs in severe COVID-19 PMNs, compared to (E) HC PMNs and (F) severe COVID-19 LDGs.

(G-H) Volcano plots of (G) severe COVID-19 PMNs versus mild COVID-19 PMNs and (H) mild COVID-19 PMNs vs HC PMN. Blue points represent significant terms (adjusted p-value < 0.05), while smaller gray points represent non-significant terms. Relevant inflammasome related or predicted genes based on the literature, according to GENESHOT, are shown with a larger and darker blue point.

DEG = differentially expressed genes.

1054 **Supplementary Figure 2. Differential expression of interferon and inflammasome related genes in**  
1055 **PMNs during COVID-19.** RNA was extracted from isolated HC PMNs (n = 8-13) versus severe COVID-  
1056 19 PMNs (n = 29-32) and subjected to comparative RT-qPCR using specific primers for OAS1, OAS2,  
1057 IFIT1, IFI16, caspase1, caspase5, IL1B, NLRC4, NLRC5, NLRP3 and NAIP. \*p < 0.05, \*\*p < 0.01, \*\*\*p  
1058 < 0.001 and \*\*\*\* p < 0.0001. P values calculated with Mann-Whitney U-test. Data presented as mean ±  
1059 SD.  
1060  
1061

1062  
1063  
1064  
1065  
1066  
1067  
1068  
1069  
1070  
1071  
1072  
1073  
1074  
1075  
1076  
1077

**Supplementary Figure 3. *Ex vivo* stimulation of isolated PMNs.**

(A-C) Effect of different inflammasome specific inhibitors in cytokine secretion. (A) Effect of inflammasome inhibitor MCC950 (2 µg/ml) and YVAD (20 µg/ml) on LPS or IFN-I primed (4-h) and nigericin activated (4-h) IL-1β secretion in the supernatant of healthy control PMNs (n = 8). (B-C) Effect of inflammasome inhibitor MCC950 (2 µg/ml, added simultaneously with nigericin) on LPS or IFN-I primed (4-h) and nigericin activated (20-h) (B) IL-1β and (C) IL-18 secretion in the supernatant of healthy control PMN (n = 3).

(D) Gene expressions in HC and COVID-19 PMNs after LPS or IFN-I stimulation. A comparison of gene expression in isolated healthy control PMNs versus COVID-19 PMNs after *ex vivo* stimulation with LPS or IFN-I. Extracted RNA was subjected to comparative RT-qPCR using specific primers for NLRP3, NLRC4, NAIP and CASP5 (n = 4-8 for HC PMN and 6-9 for COVID-19 PMN). \*p < 0.05. Two-way ANOVA with Tukey's multiple comparison test was applied. Data were presented as mean ± SD.

\*p < 0.05, \*\*p < 0.01, \*\*\*p < 0.001, \*\*\*\*p < 0.0001. P values calculated with Kruskal-Wallis test. Data presented as mean ± SD. *IFN* = interferon type I, *LPS* = lipopolysaccharide, *Nig* = nigericin, *YVAD* = tetrapeptide caspase1 inhibitor Tyr-Val-Ala-Asp.

1078  
1079  
1080  
1081  
1082  
1083  
1084

**Supplementary Figure 4. Expression of inflammasome related genes in mature and immature neutrophils from COVID-19 PBMCs.** The fraction of mature and immature neutrophils cells expressing 17 inflammasome related genes identified in Figure 7B (shown in black and blue, respectively) are shown in a bar graph. For each gene, the proportion of expressing cells is shown in light blue, while the proportion of negative or not-expressing cells is shown in gray. Zoomed-in bar graph depicts the proportion of mature and immature cells expressing each gene.

1085 **Supplementary Figure 5. Dynamics of animal weight and impact of  $\alpha$ -IFNAR treatment in SARS-**  
1086 **CoV-2 infected mice.** Female BALB/c mice were intranasally inoculated with  $5 \times 10^5$  TCID50 SARS-  
1087 CoV-2 MaVie strain or PBS as control.  
1088 (A) Daily tracking of animal weight performed throughout the experiment (n = 8 for SARS-CoV-2  
1089 infected animals, n = 2 for PBS-inoculated animals). The weights of the mice euthanized at 2 dpi (n= 26)  
1090 did not show significant differences and are not reported.  
1091 (B-C) Mice were intraperitoneally inoculated with 250  $\mu$ g anti-IFNAR or IgG1 isotype control directly  
1092 after infection with SARS-CoV-2 and lung neutrophils isolated at 2 dpi (including also intranasally PBS-  
1093 inoculated control mice without intraperitoneal injection)  
1094 (B) RNA was isolated from mouse lungs and subjected to RT-qPCR targeting the replication-intermediate  
1095 subgenomic E gene and GAPDH as housekeeping gene. RNA levels were assessed based on cycle  
1096 threshold Ct levels. The expression levels of the target gene SubE were measured and normalized to  
1097 GAPDH levels using the comparative Ct method ( $\Delta\Delta$ Ct). The fold change values were calculated by the  
1098 formula  $2^{-(\Delta\Delta$ Ct)}, representing the relative gene expression compared to the PBS mock-infected control  
1099 (in which subE was undetectable but set to 40 Ct). No significant differences are seen between the two  
1100 groups.  
1101 (C) Histological features, viral antigen expression and extent of neutrophil influx and damage in the lung  
1102 of SARS-CoV-2 infected BALB/C mice after isotype control and anti-IFNAR treatment at 2dpi.  
1103 Left column: Control isotype treated mice; right column: anti-IFNAR treated mice. HE stain (top layer)  
1104 and immunohistology, hematoxylin counterstain (all other images). Bars: 250  $\mu$ m (overview images) and  
1105 25  $\mu$ m (insets).  
1106 In control isotype treated mice, the lung exhibits degeneration and loss of bronchial and bronchiolar  
1107 epithelial cells (HE stain: arrowhead; right inset), with mild inflammatory infiltration. The parenchyma  
1108 exhibits focal areas of increased cellularity, with typeII pneumocyte activation and occasional degenerate  
1109 alveolar epithelial cells (arrows; left inset: degenerate cells (arrowhead) and infiltrating neutrophil  
1110 (arrow)). Staining for SARS-CoV-2 NP confirms epithelial cell infection in bronchus (arrowhead; right  
1111 inset) and alveoli (arrow; left inset). Right inset: Viral antigen expression is seen in intact and sloughed  
1112 off, degenerate epithelial cells. Left inset: Viral antigen expression is seen in both typeI (small arrowhead)  
1113 and typeII (small arrow) pneumocytes; there are also degenerate positive cells (large arrowhead).  
1114 Neutrophils (Ly6G+) are located within focal parenchymal areas of increased cellularity (arrows; left  
1115 inset: arrowheads) and present between degenerate bronchial epithelial cells (arrowhead; right inset:  
1116 arrowhead). Staining for histone H3 shows neutrophil degeneration/NETosis in parenchymal areas  
1117 (arrow; left inset: arrowheads) and associated with degenerate epithelial cells (arrowhead; right inset:  
1118 positive reaction between sloughed off epithelial cells (arrow) and between the intact epithelial layer  
1119 (arrowhead)).  
1120 In anti-IFNAR treated animals, the lung exhibits degeneration and loss of bronchial and bronchiolar  
1121 epithelial cells (arrowhead; right inset: arrows), with mild inflammatory infiltration and individual  
1122 neutrophils between intact and sloughed off degenerate epithelial cells (right inset: arrowheads). The  
1123 parenchyma exhibits focal areas of increased cellularity, with typeII pneumocyte activation and occasional  
1124 degenerate alveolar epithelial cells (arrows; left inset: degenerate cells (arrow) and infiltrating neutrophils  
1125 (arrowhead). Staining for SARS-CoV-2 NP shows epithelial cell infection in bronchioles (arrowhead;  
1126 right inset) and alveoli (arrow; left inset). Right inset: Viral antigen expression is seen in intact and  
1127 sloughed off, degenerate epithelial cells. Left inset: Viral antigen expression is seen in pneumocytes  
1128 (arrow) and infiltrating macrophages (arrowheads). Neutrophils (Ly6G+) locate within focal parenchymal  
1129 areas of increased cellularity (arrows; left inset) and are present between intact (inset: arrowhead) and  
1130 degenerate epithelial cells (arrowhead; right inset: arrow). Staining for histone H3 shows neutrophil  
1131 degeneration/NETosis in parenchymal areas (arrow; left inset) and associated with degenerate epithelial  
1132 cells (arrowhead; right inset: positive reaction between sloughed off epithelial cells (arrow) and between  
1133 the intact epithelial layer (arrowhead)).  
1134 *Dpi= days post infection; NP = nucleoprotein.*

1135  
1136  
1137  
1138

## Table legends

**Table 1. Clinical parameters of hospitalized patients (n=34).**

Parameter	Range (Mean $\pm$ SD) or ratio
Age (years)	22 - 80 (58.41 $\pm$ 13.63)
Gender (male:female)	23:11
Hospitalization (days)	3 - 38 (12 $\pm$ 8.63)
WHO Ordinal scale for Clinical improvement: Baseline	1 - 6 (4 $\pm$ 1.07)
WHO Ordinal scale for Clinical improvement: Worst	2 - 8 (4 $\pm$ 1.42)
Deaths (count/total)	1/34
ICU (count/total)	9/34
Corticosteroid use (count/total)	13/34
Length of stay in ICU (days)	1 - 27 (7.38 $\pm$ 9.49)
Max CRP (mg/L)	6 - 466 (159.56 $\pm$ 104.06)
Min lymphocyte count (E <sup>9</sup> /L)	0.08 - 2.02 (0.79 $\pm$ 0.42)
Max neutrophil count (E <sup>9</sup> /L)	1.08 - 29.86 (7.85 $\pm$ 5.73)
Sampling day neutrophil count (E <sup>9</sup> /L)	0.64 - 20.52 (5.65 $\pm$ 3.95)

1139  
1140  
1141  
1142  
1143  
1144  
1145  
1146  
1147  
1148  
1149  
1150

The World Health Organization (WHO) Ordinal Scale for clinical improvement is a tool designed specifically to assess and measure the progression and clinical improvement of patients<sup>63</sup>. COVID-19 scoring: 1= no limitations of activity, 2= limitations of activity, 3= no oxygen therapy, 4= oxygen by mask or nasal cannulae, 5= non-invasive ventilation or high-flow oxygen, 6= invasive mechanical ventilation without other organ support, 7= invasive mechanical ventilation with other organ support, 8= dead. The baseline score represents the timepoint of the first laboratory sample taken, serving as a reference point for measuring improvement and establishing a starting point for comparison. In contrast, the worst score represents the most severe or critical state of the disease. None of the patients whose samples were used for RNA-seq underwent corticosteroid treatment. *Abbreviations: WHO= World Health Association. ICU = Intensive Care Unit. CRP = C reactive protein. Min = minimum. Max = maximum.*

1151  
1152

**Supplementary Table S1. qPCR primer sequences: gene-specific forward and reverse primers.**

Gene	Forward primer	Reverse primer
<b>AIM2</b>	GGCCCAGCAGGAA TCTATCAG	GAAGGGCTTCTTTGCTTTCAGTAC
<b>NAIP</b>	AAGGGATTGTTGACATAACGGG	CAGCCGTAGTTCTTCGTAAGC
<b>NLRC5</b>	ACAGCATCCTTAGACACTCCG	CCTTCCCCAAAAGCACGGT
<b>IL1B</b>	CACATGGGATAACGAGGCTT	TCCAGCTGTAGAGTGGGCTT
<b>CASP1</b>	GCTTTCTGCTCTCCACACC	TCCTCCACATCACAGGAACA
<b>CASP4</b>	CAAGAGAAGCAACGTATGGCA	AGGCAGATGGTCAAACCTCTGTA
<b>CASP5</b>	TTCAACACCACATAACGTGTCC	GTCAAGGTTGCTCGTTCTATGG
<b>IFI16</b>	TCCTCAGATGCCTCCATCAAC	CAGGTCAGTCTTCAGTCTTGGT
<b>IFIT5</b>	TAAAAAAGGCCTTGGAGGTG	CCAGGTCTGTGTAGGCAAAT
<b>IRF7</b>	GCTGGACGTGACCATCATGTA	GGGCCGTATAGGAACGTGC
<b>IFIT1</b>	GCGCTGGGTATGCGATCTC	CAGCCTGCCTTAGGGGAAG
<b>IFI6</b>	GGTCTGCGATCCTGAATGGG	TCACTATCGAGATACTTGTGGGT
<b>OAS1</b>	TGTCCAAGGTGGTAAAGGGTG	CCGGCGATTTAACTGATCCTG
<b>OAS2</b>	CTCAGAAGCTGGGTTGGTTTAT	ACCATCTCGTCGATCAGTGTC
<b>GAPDH</b>	TTGGCTACAGCAACAGGGTG	GGGGAGATTCAGTGTGGTGG

1153  
1154

1155  
1156  
1157

**Supplementary Table S2. Histological changes as well as SARS-CoV-2 nucleoprotein and RNA expression in female BALB/C mice infected with SARS-CoV-2.**

**A. Experiment 1.** Infected animals were euthanized and examined at 2 and 4 days post infection.

Infection, dpi [Animal no]	Histological changes, viral antigen and Ly6G expression <sup>1</sup> in lungs	Viral subE (and GAPDH) RNA Cts <sup>2</sup>
<b>5 x 10<sup>5</sup> PFU, 2 dpi</b> [1.1.1]	<b>HE:</b> bronchioles with abundant degen EC (in place and sloughed off); parenchymal areas with type II pn activation, occ degen AEC and increased cellularity <b>vAg:</b> extensive expression in bronchus/bronchioles (almost all BEC, some also degen); most alveoli with pos AEC <b>Ly6G:</b> increase in NL in lumen of vessels and capillaries; NL in lumen of bronchioles and alveoli (partly degen) and in association with degen BEC	15.12 (13.47)
<b>5 x 10<sup>5</sup> PFU, 2 dpi</b> [1.1.2]	<b>HE:</b> bronchioles with abundant degen EC (in place and sloughed off); parenchymal areas with type II pn activation, occ degen AEC and increased cellularity <b>vAg:</b> extensive expression in bronchus/bronchioles (almost all BEC, some also degen); most alveoli with pos AEC <b>Ly6G:</b> increase in NL in lumen of vessels and capillaries, NL in lumen of bronchioles and alveoli (partly degen) and in association with degen BEC	15.92 (13.79)
<b>5 x 10<sup>5</sup> PFU, 2 dpi</b> [1.1.3]	<b>HE:</b> bronchioles with abundant degen EC (in place and sloughed off); parenchymal areas with type II pn activation, occ degen AEC and increased cellularity <b>vAg:</b> extensive expression in bronchus/bronchioles (almost all BEC, some also degen); most alveoli with pos AEC <b>Ly6G:</b> increase in NL in lumen of vessels and capillaries, NL in lumen of bronchioles and alveoli (partly degen) and in association with degen BEC	15.56 (13.83)
<b>5 x 10<sup>5</sup> PFU, 2 dpi</b> [1.1.4]	<b>HE:</b> bronchioles with abundant degen EC (in place and sloughed off); parenchymal areas with type II pn activation, occ degen AEC and increased cellularity <b>vAg:</b> extensive expression in bronchus/bronchioles (almost all BEC, some also degen); most alveoli with pos AEC <b>Ly6G:</b> increase in NL in lumen of vessels and capillaries, NL in lumen of bronchioles and alveoli (partly degen)	16.33 (14.81)
<b>5 x 10<sup>5</sup> PFU, 4 dpi</b> [1.2.1]	<b>HE:</b> one bronchiole with degen EC (in place and sloughed off), others unaltered; large parenchymal area with extensive type II pn activation, degen AEC and increased cellularity (leukocytes incl NL) <b>vAg:</b> some bronchioles with extensive expression (almost all BEC, some also degen), others with a few individual or no pos BEC; patches of alveoli with pos AEC (within and outside affected areas) <b>Ly6G:</b> some increase in NL in lumen of vessels and capillaries, NL in lumen of bronchioles and alveoli in affected area (partly degen)	31.68 (11.64)
<b>5 x 10<sup>5</sup> PFU, 4 dpi</b> [1.2.2]	<b>HE:</b> bronchioles with a few degen EC (in place or sloughed off), others unaltered; small parenchymal area with type II pn activation, degen AEC and increased cellularity (leukocytes incl NL) <b>vAg:</b> some bronchioles with several (partly degen) pos BEC, most with a few individual or no pos BEC; patches of alveoli with pos AEC (within and outside affected area) <b>Ly6G:</b> some increase in NL in lumen of vessels and capillaries, a few NL in lumen of bronchioles and alveoli in affected area (partly degen)	31.86 (11.78)
<b>5 x 10<sup>5</sup> PFU, 4 dpi</b> [1.2.3]	<b>HE:</b> bronchioles with a few degen EC (in place or sloughed off), others unaltered; small parenchymal area with type II pn activation, degen AEC and increased cellularity (leukocytes incl NL) <b>vAg:</b> some bronchioles with several (partly degen) pos BEC, most with a few individual or no pos BEC; patches of alveoli with pos AEC (within and outside affected area) <b>Ly6G:</b> some increase in NL in lumen of vessels and capillaries, a few NL in lumen of bronchioles and alveoli in affected area (partly degen)	31.33 (11.71)
<b>5 x 10<sup>5</sup> PFU, 4 dpi</b> [1.2.4]	<b>HE:</b> bronchioles with rare degen EC, most unaltered; parenchymal area with type II pn activation, degen AEC and increased cellularity (leukocytes incl NL) <b>vAg:</b> some bronchioles with a few to several (partly degen) pos BEC, most with a few individual or no pos BEC; patches of alveoli with pos AEC (within and outside affected area) <b>Ly6G:</b> some increase in NL in lumen of vessels and capillaries, a few NL in lumen of bronchioles and alveoli in affected area (partly degen)	35.02 (11.89)
<b>PBS (control), 2 dpi</b> [1.3.1]	<b>Lung:</b> NHA <b>vAg:</b> neg <b>Ly6G:</b> a few individual NL in lumen of vessels and capillaries	n.d., set to 40 (13.65)
<b>PBS (control), 2 dpi</b> [1.3.2]	<b>Lung:</b> NHA <b>vAg:</b> neg <b>Ly6G:</b> a few individual NL in lumen of vessels and capillaries	n.d., set to 40 (15.66)



<b>PBS (control), 2 dpi</b> [1.3.3]	<b>Lung:</b> NHA <b>vAg:</b> neg <b>Ly6G:</b> a few individual NL in lumen of vessels and capillaries	n.d., set to 40 (14.32)
<b>PBS (control), 2 dpi</b> [1.3.4]	<b>Lung:</b> NHA <b>vAg:</b> neg <b>Ly6G:</b> a few individual NL in lumen of vessels and capillaries	n.d., set to 40 (14.57)

1158

1159

1160

**B. Experiment 3.** Infected animals were treated with control isotype or IFNAR blocking antibody prior to euthanization and examination at 2 days post infection.

<b>Infection, treatment</b> [Animal no, sex, age]	<b>Histological changes, viral antigen (vAg), Ly6G and histone H3 expression<sup>1</sup> in lungs</b>	<b>Viral subE (and GAPDH) RNA Cts<sup>2</sup></b>
<b>5 x 10<sup>5</sup> PFU, control isotype</b> [3.1.1]	<b>HE:</b> bronchus and connected bronchiole with abundant degen EC (in place or sloughed off); endothelial cell activation in adjacent muscular veins, with some leukocyte adhesion; adjacent parenchymal areas with type II pn activation, occ degen AEC and increased cellularity <b>vAg:</b> extensive expression in bronchus/bronchioles (almost all BEC, also degen), and large adjacent areas of alveoli with pos AEC <b>Ly6G:</b> increase in NL in lumen of vessels and capillaries in affected areas, NL in lumen of bronchioles and alveoli (partly degen) <b>H3:</b> pos reaction in areas with degen NL (lumen of bronchioles, affected alveoli)	14.75 (12.63)
<b>5 x 10<sup>5</sup> PFU, control isotype</b> [3.1.2]	<b>HE:</b> some bronchioles with abundant degen EC (in place or sloughed off); endothelial cell activation in some adjacent vessels; (adjacent) parenchymal areas with type II pn activation, occ degen AEC and increased cellularity <b>vAg:</b> extensive expression in some bronchioles (almost all BEC, also degen), large (adjacent) areas of alveoli with pos AEC <b>Ly6G:</b> mild increase in NL in lumen of vessels and capillaries in affected areas, NL in lumen of bronchioles and alveoli (partly degen) <b>H3:</b> pos reaction in areas with degen NL (lumen of bronchioles, affected alveoli)	16.61 (11.54)
<b>5 x 10<sup>5</sup> PFU, control isotype</b> [3.1.3]	<b>HE:</b> bronchioles with abundant degen EC (in place or sloughed off); endothelial cell activation in some muscular veins, with leukocyte rolling and subendothelial infiltration (vasculitis), other vessels packed with leukocytes; (adjacent) parenchymal areas with type II pn activation, occ degen AEC and increased cellularity <b>vAg:</b> extensive expression in bronchioles (patches of BEC to almost all BEC, also degen), large (adjacent) areas of alveoli with pos AEC <b>Ly6G:</b> mild increase in NL in lumen of vessels and capillaries in affected areas, NL in lumen of bronchioles and alveoli (often degen) <b>H3:</b> extensive pos reaction in areas with degen NL (lumen of bronchioles, affected alveoli)	16.00 (12.71)
<b>5 x 10<sup>5</sup> PFU, control isotype</b> [3.1.4]	<b>HE:</b> bronchus and bronchioles with abundant degen EC (in place or sloughed off); endothelial cell activation in some muscular veins, with leukocyte rolling and pv infiltration; (adjacent) parenchymal areas with type II pn activation, occ degen AEC and increased cellularity <b>vAg:</b> extensive expression in bronchioles (patches to almost all BEC, also degenerate), large (adjacent) areas of alveoli with pos AEC <b>Ly6G:</b> mild increase in NL in lumen of vessels and capillaries in affected areas, NL in lumen of bronchioles and alveoli (partly degenerate) <b>H3:</b> pos reaction in areas with degen NL (lumen of bronchioles, affected alveoli); most extensive in alveoli	15.07 (13.83)
<b>5 x 10<sup>5</sup> PFU, anti-IFNAR</b> [3.2.1]	<b>HE:</b> bronchus and connected bronchiole with abundant degen EC (in place or sloughed off); endothelial cell activation in muscular veins, with some leukocyte adhesion; patchy parenchymal areas with type II pn activation, occ degen AEC and increased cellularity <b>vAg:</b> extensive expression in bronchioles (abundant to almost all BEC, also degen), and large areas of alveoli with pos AEC <b>Ly6G:</b> increase in NL in lumen of vessels and capillaries in affected areas, NL in lumen of bronchioles and alveoli (partly degen) <b>H3:</b> pos reaction in areas with degen NL (lumen of bronchioles, affected alveoli)	13.98 (12.44)
<b>5 x 10<sup>5</sup> PFU, anti-IFNAR</b> [3.2.2]	<b>HE:</b> bronchioles with occ degen EC (in place or sloughed off); endothelial cell activation in muscular veins, with some leukocyte adhesion; parenchymal areas with type II pn activation, occ degen AEC and increased cellularity <b>vAg:</b> extensive expression in bronchus/bronchioles (almost all BEC, also degen), and large areas of alveoli with pos AEC <b>Ly6G:</b> increase in NL in lumen of vessels and capillaries in affected areas, NL in lumen of bronchioles and alveoli (partly degen) <b>H3:</b> pos reaction in areas with degen NL (lumen of bronchioles, affected alveoli)	14.90 (13.12)

<b>5 x 10<sup>5</sup> PFU, anti-IFNAR</b> [3.2.3]	<b>HE:</b> infected bronchus with a few degen EC (in place); mild endothelial cell activation in some adjacent vessels; (adjacent) parenchymal areas with type II pn activation and increased cellularity <b>vAg:</b> a few individual EC in bronchus and some bronchioles, one with all EC pos, adjacent large patches of alveoli with pos AEC <b>Ly6G:</b> increase in individual NL in lumen of vessels and capillaries (mainly in affected areas), a few NL in lumen and between EC of infected bronchiole, and in alveoli in affected areas <b>H3:</b> rare pos reaction in alveoli	28.79 (14.09)
<b>5 x 10<sup>5</sup> PFU, anti-IFNAR</b> [3.2.4]	<b>HE:</b> infected bronchioles with variable amount of degen EC (in place or sloughed off); endothelial cell activation in some vessels, with leukocyte rolling and pv infiltration; (adjacent) parenchymal areas with type II pn activation, occ degen AEC and increased cellularity <b>vAg:</b> bronchus and bronchioles with individual, patches of to almost all BEC pos (also degen) and cell free viral Ag in lumen, large (adjacent) areas of alveoli with pos AEC (also degen) <b>Ly6G:</b> increase in NL in lumen of vessels and capillaries in affected areas, NL in lumen of bronchioles and alveoli (partly degen) <b>H3:</b> extensive pos reaction in areas with degen NL (lumen of bronchioles, affected alveoli)	13.54 (13.33)
<b>PBS (control), none</b> [3.3.1]	<b>Lung:</b> NHA <b>vAg:</b> neg <b>Ly6G:</b> a few individual NL in lumen of vessels and capillaries	n.d., set to 40 (10.20)
<b>PBS (control), none</b> [3.3.2]	<b>Lung:</b> NHA <b>vAg:</b> neg <b>Ly6G:</b> a few individual NL in lumen of vessels and capillaries	n.d., set to 40 (11.04)
<b>PBS (control), none</b> [3.3.3]	<b>Lung:</b> NHA <b>vAg:</b> neg <b>Ly6G:</b> a few individual NL in lumen of vessels and capillaries	n.d., set to 40 (14.06)
<b>PBS (control), none</b> [3.3.4]	<b>Lung:</b> NHA <b>vAg:</b> neg <b>Ly6G:</b> a few individual NL in lumen of vessels and capillaries	n.d., set to 40 (13.70)

1161

1162

1163

1164

1165

1166

1167

The age of the infected animals were 9 weeks in experiment 1 and 8 weeks in experiment 3; alv – alveolar; BEC – bronchiolar epithelial cells; degen – degenerate (this also includes apoptotic and/or necrotic); EC – epithelial cells; F – female; HE – histological features assessed in a hematoxylin-eosin stained section; incl – including; M – male; neg – negative; NHA – no histological abnormality; NL – neutrophilic leukocytes (i.e. neutrophils); occ – occasional; pc – pneumocytes; pos – positive; pv – perivascular; vAg – viral antigen; we – weeks; n.d. – not detected

1168

<sup>1</sup> Viral antigen and Ly6G expression determined by immunohistochemistry.

1169

1170

1171

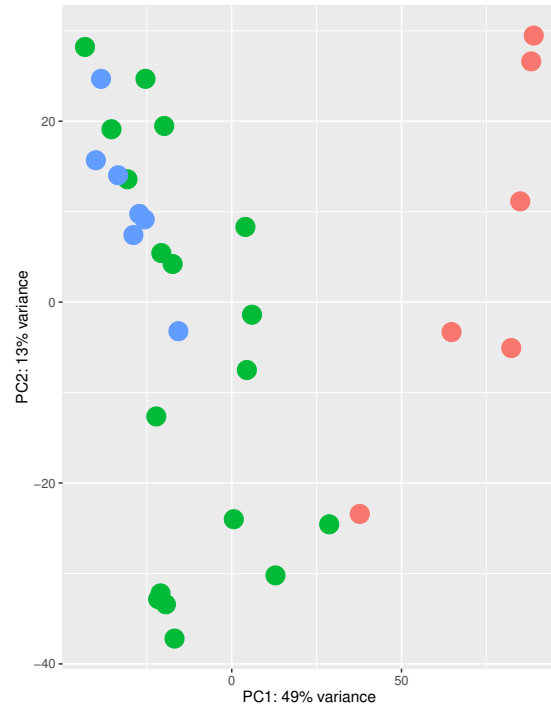
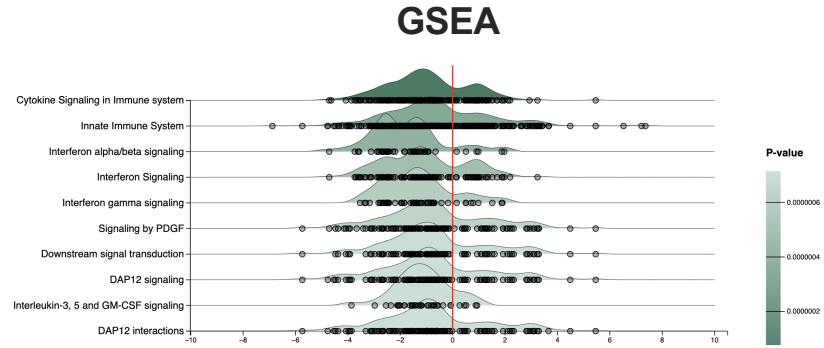
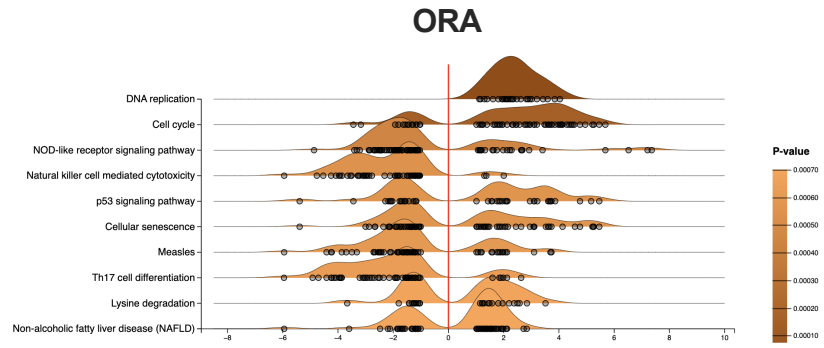
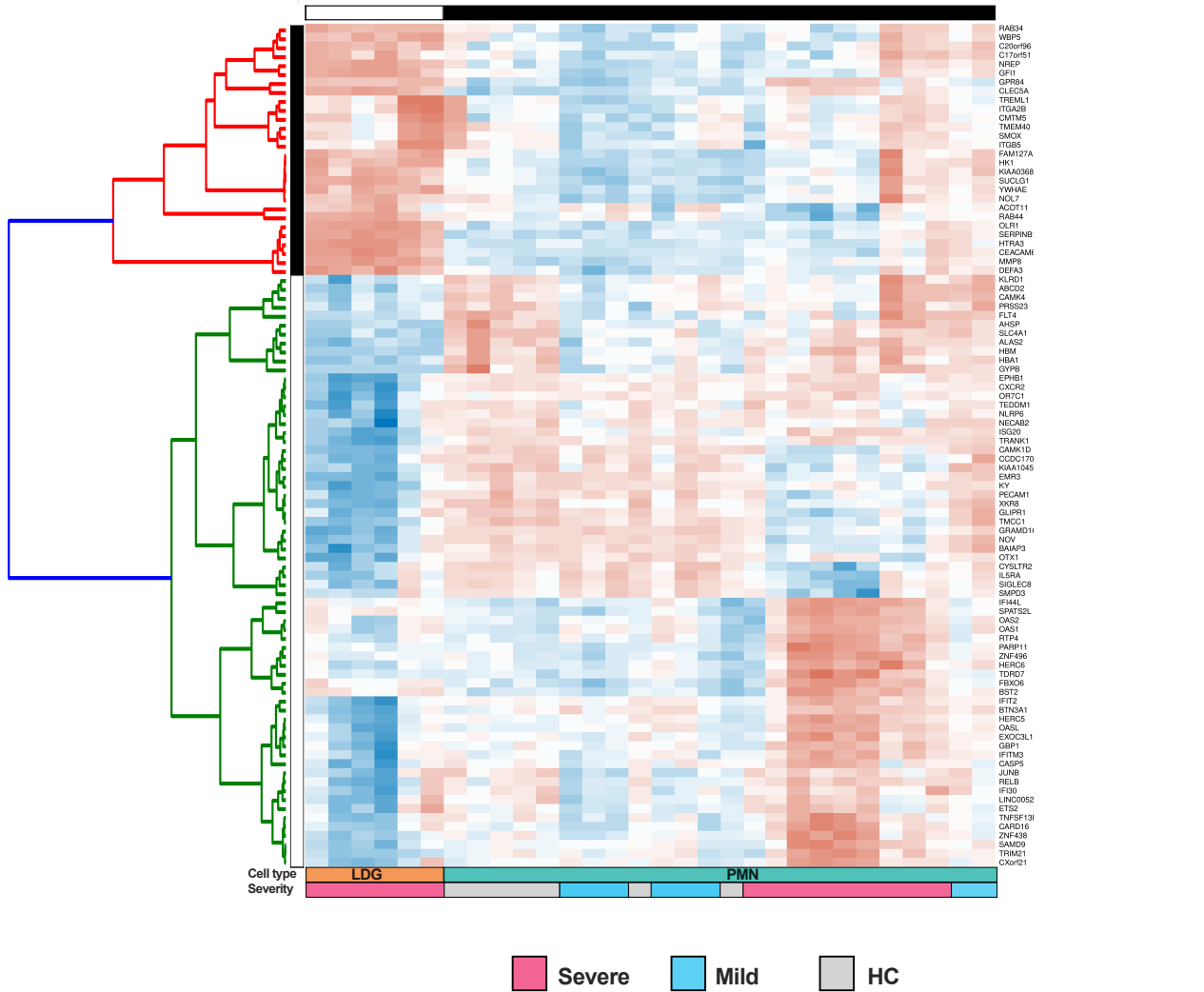
1172

<sup>2</sup> Obtained RT-qPCR cycle threshold values (Cts) for viral subgenomic E gene (subE) as a measure of viral replication and GAPDH mRNA as the housekeeping gene. As expected, for PBS control animals no Ct value for viral subE was obtained. The subE Ct for control animals was set to the detection limit of 40 to facilitate fold change calculations presented in Figure 8A and Supplementary Fig. 5B.

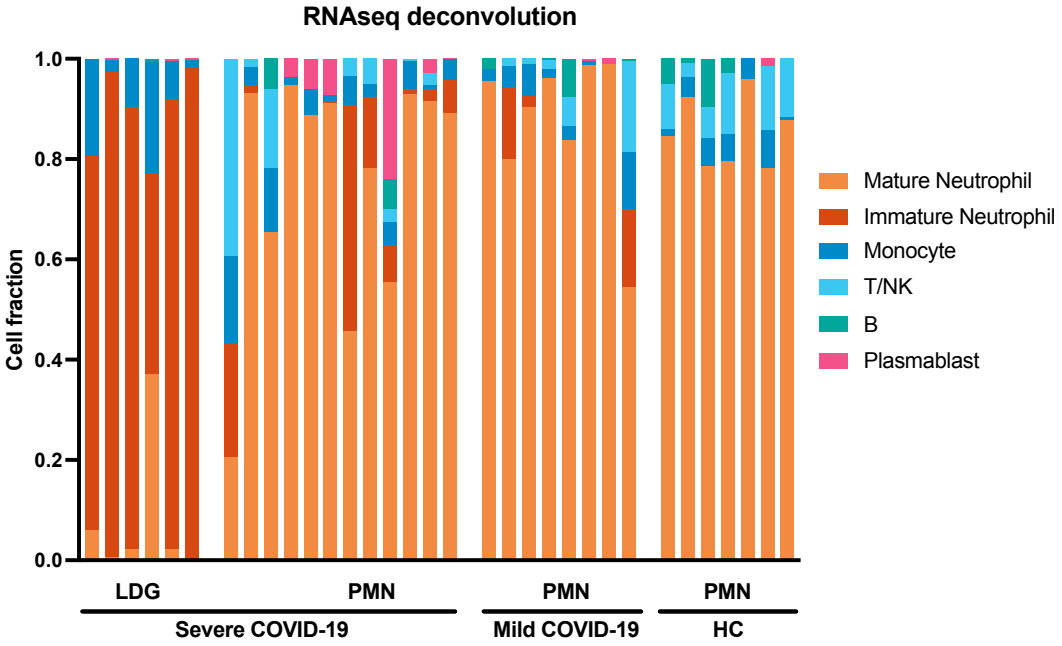
**A**

condition

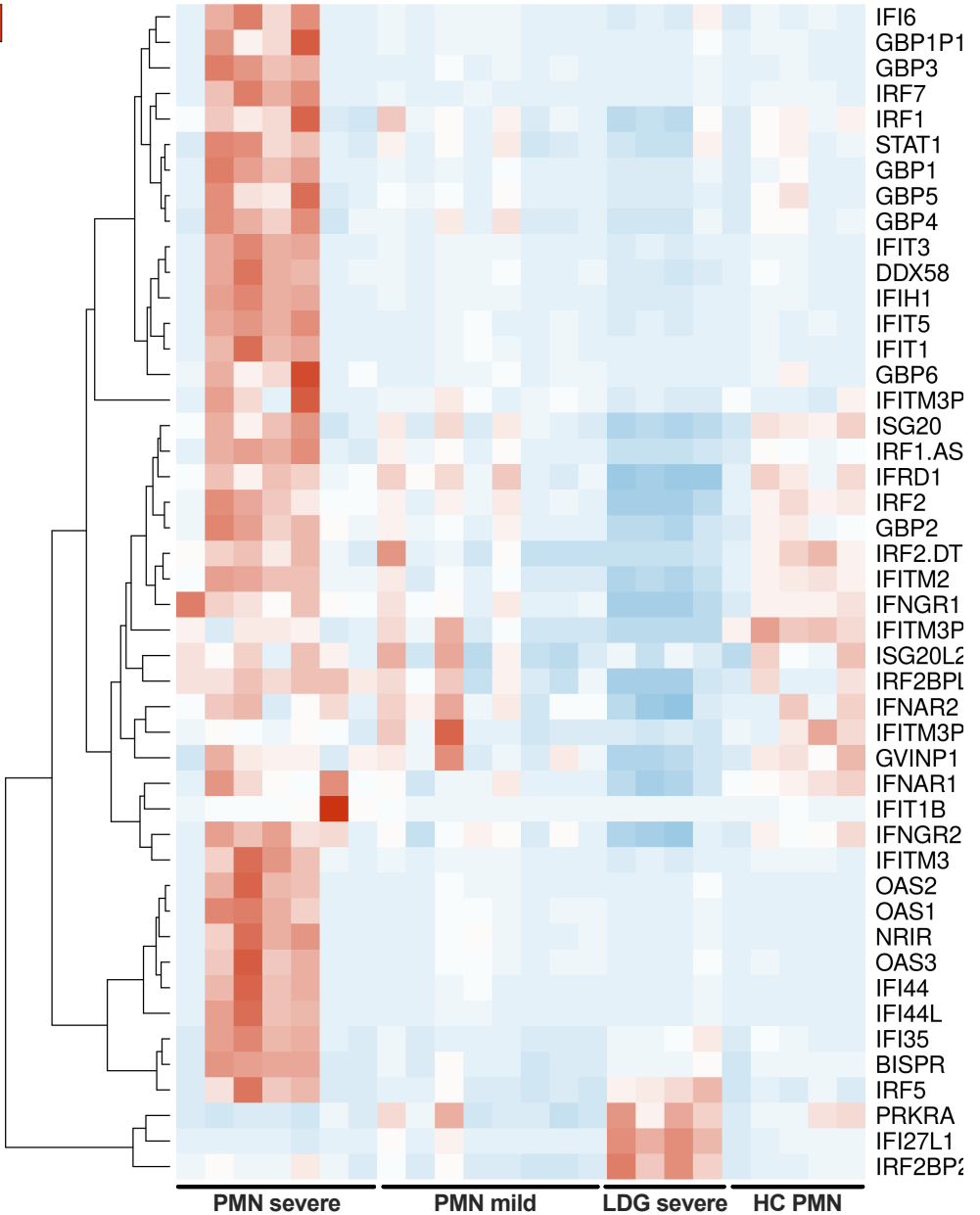
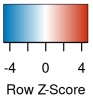
- COVID-19 LDG
- COVID-19 PMN
- HC PMN

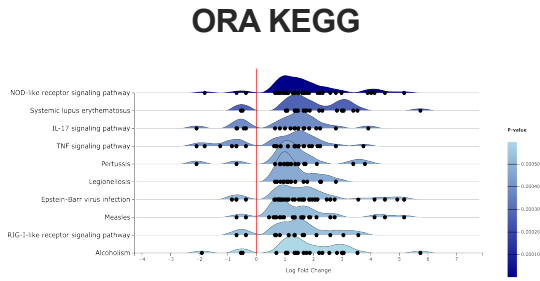
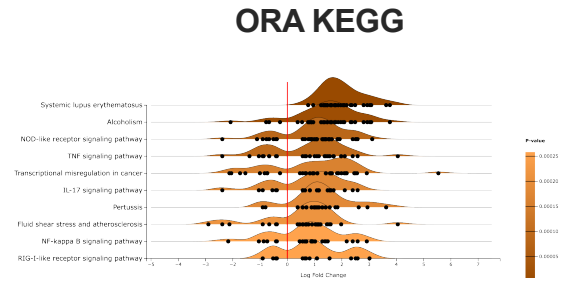
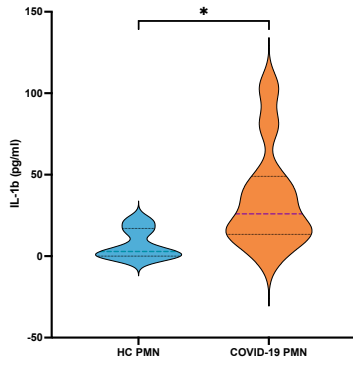
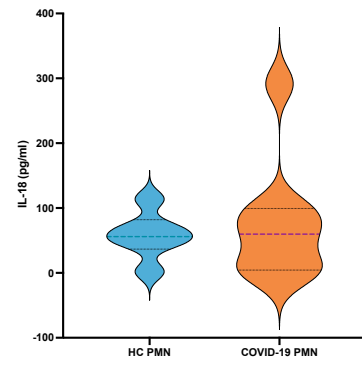
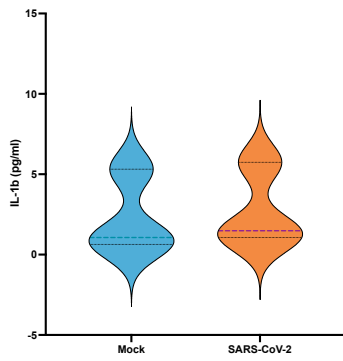
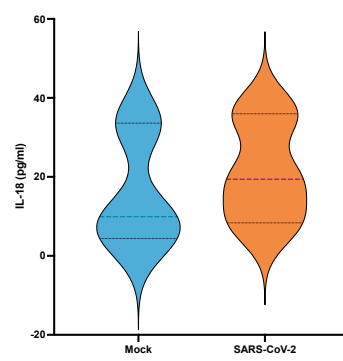
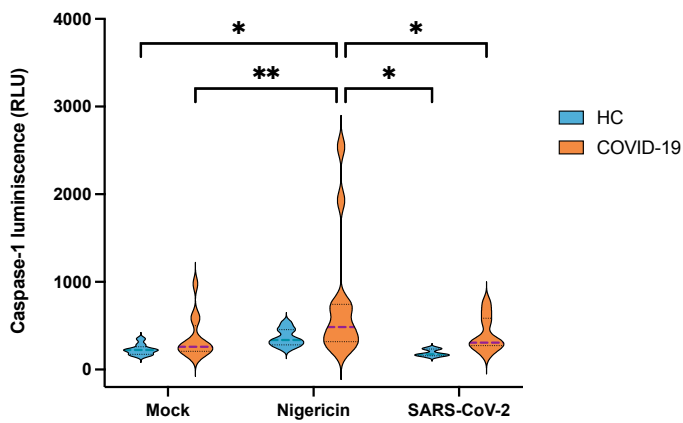
**B****C**

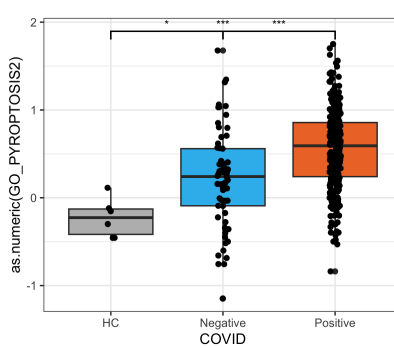
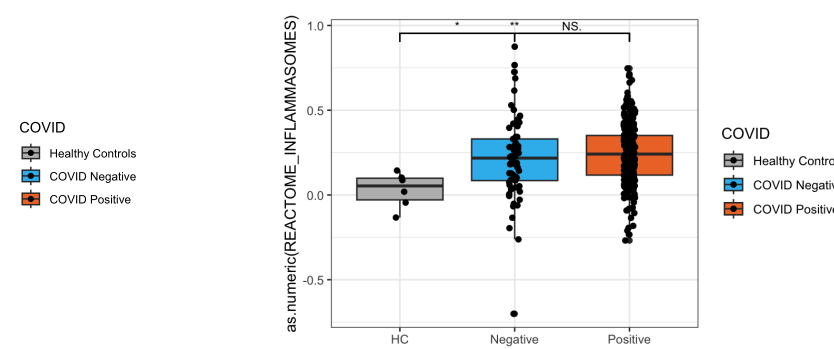
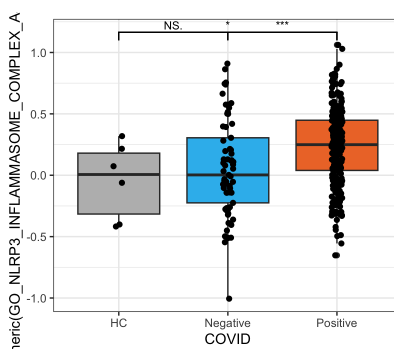
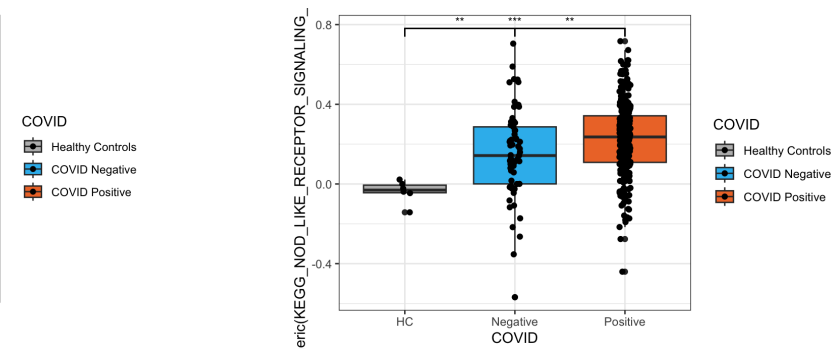
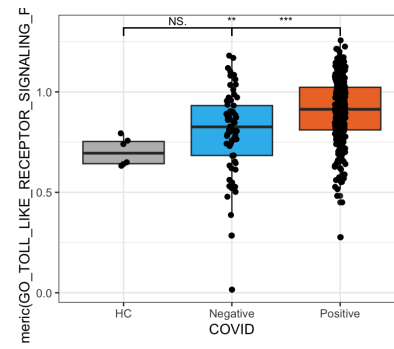
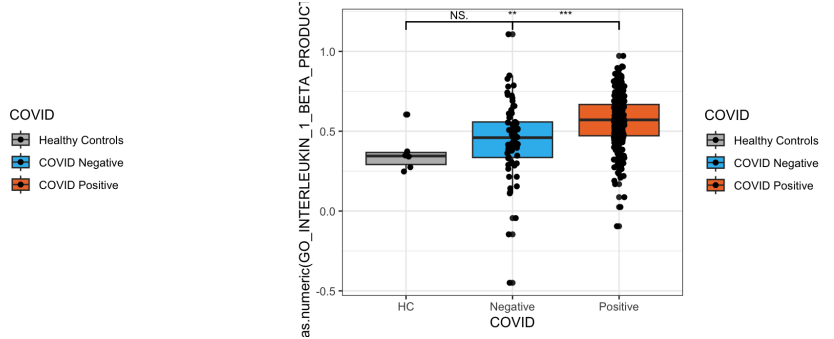
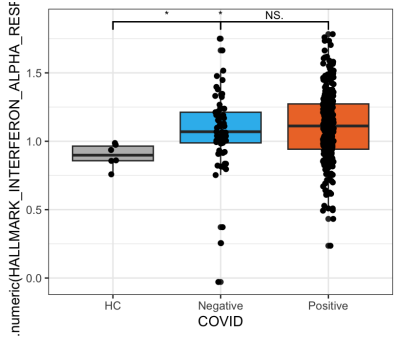
**A**



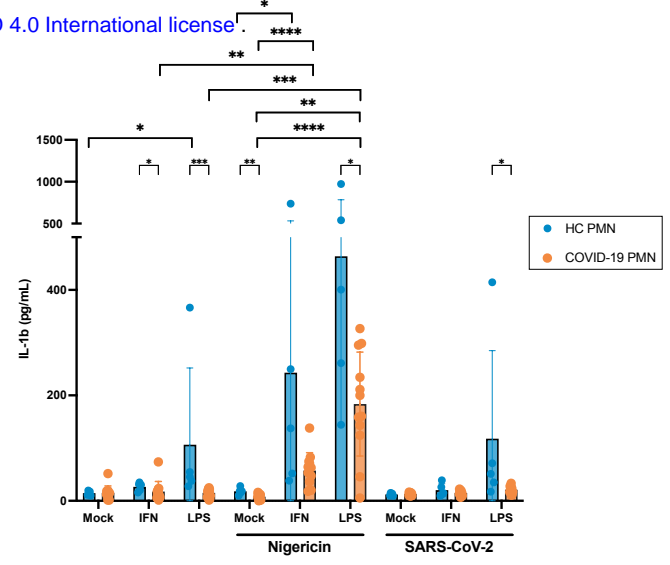
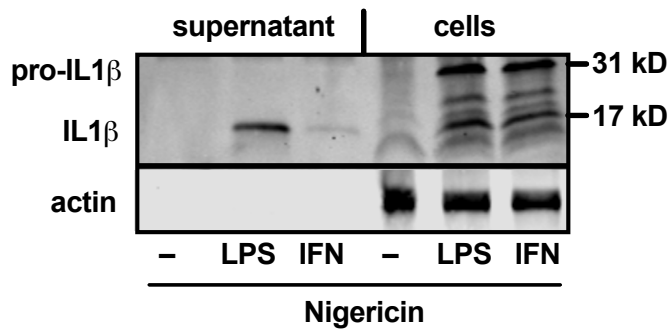
**B**



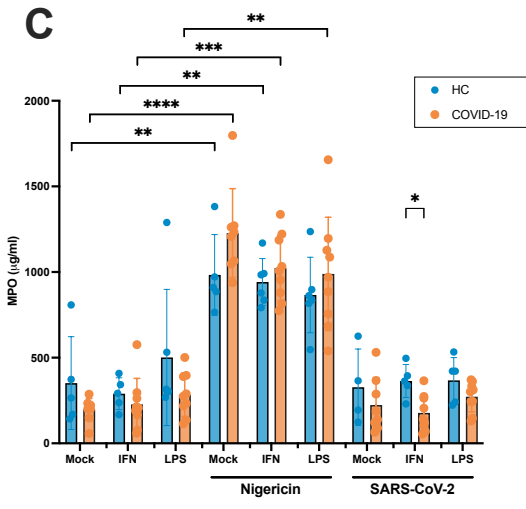
**A****B****C****D****E****F****G**



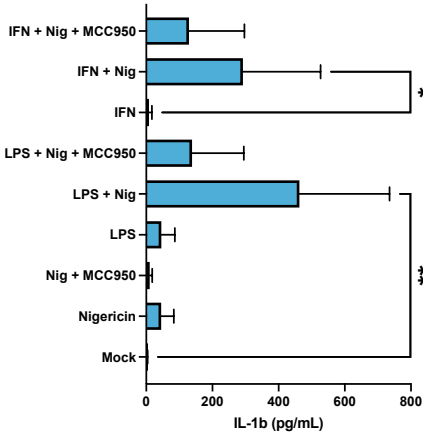
**A**



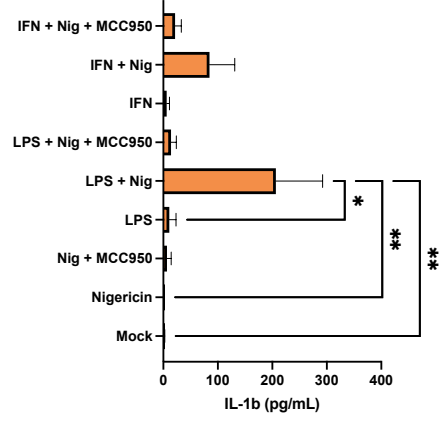
**C**



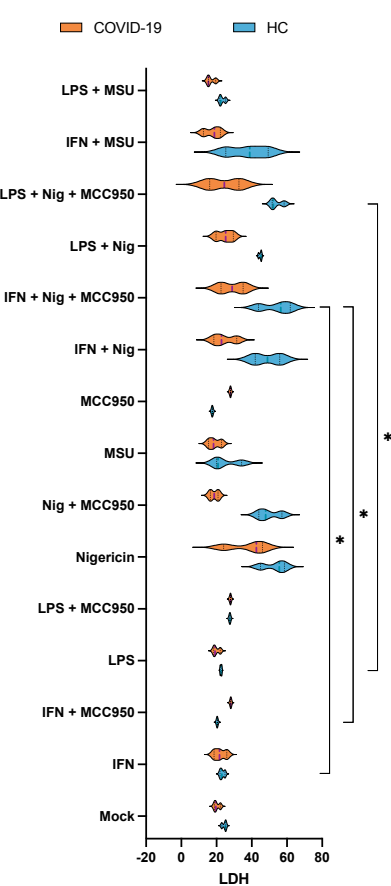
**D**



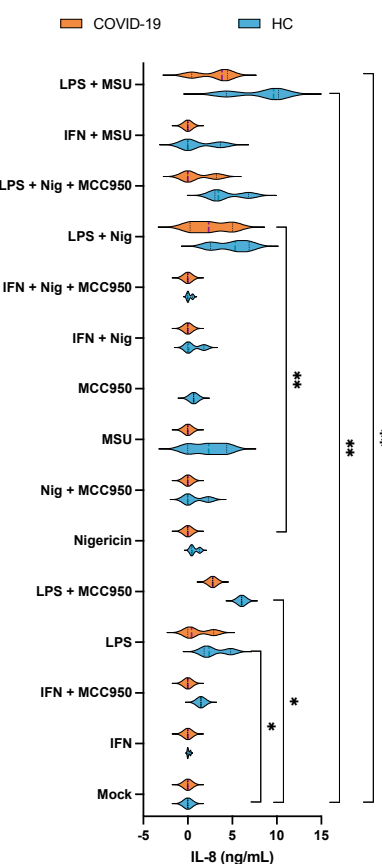
**E**



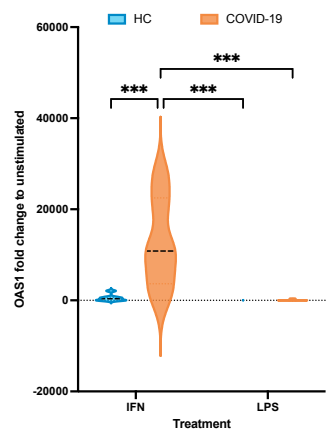
**F**



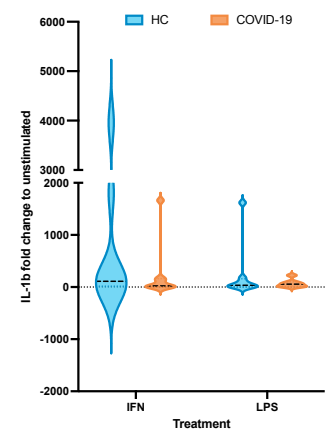
**G**



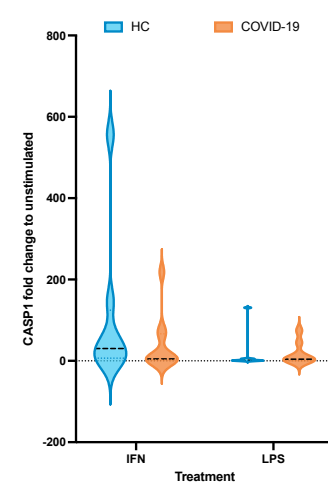
**H**



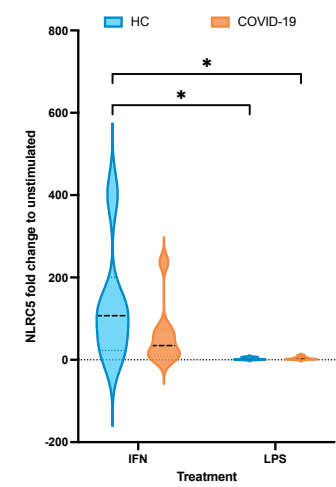
**I**

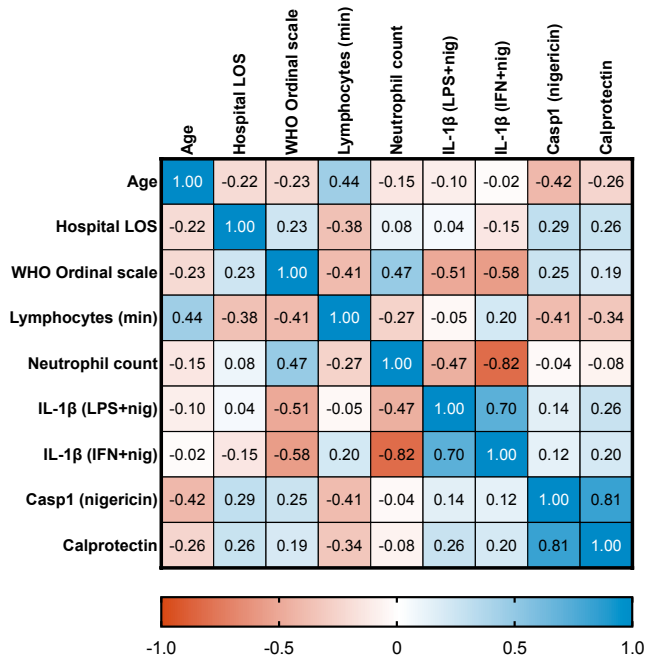
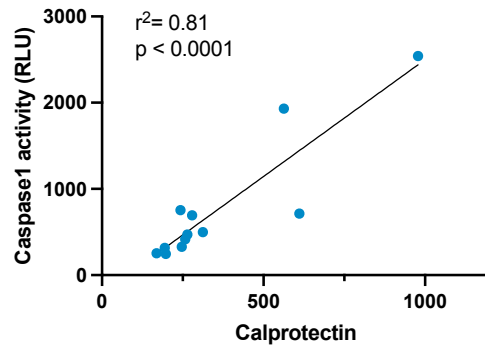
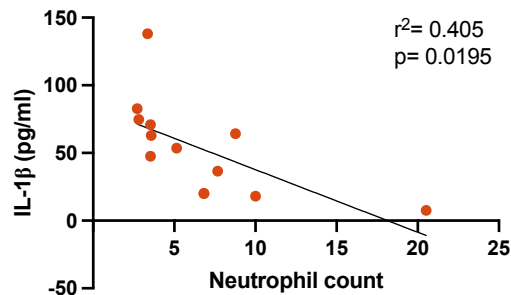


**J**

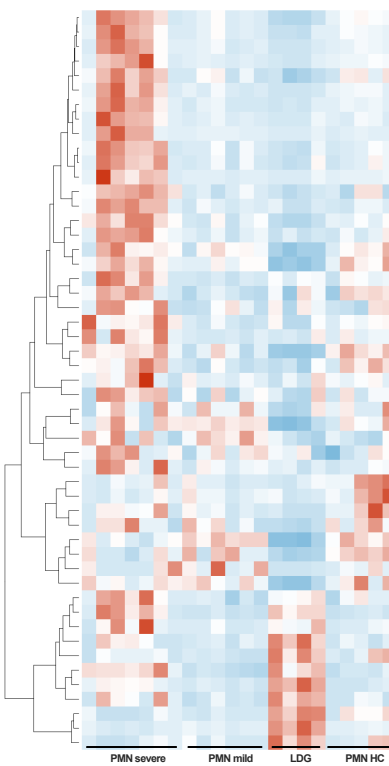
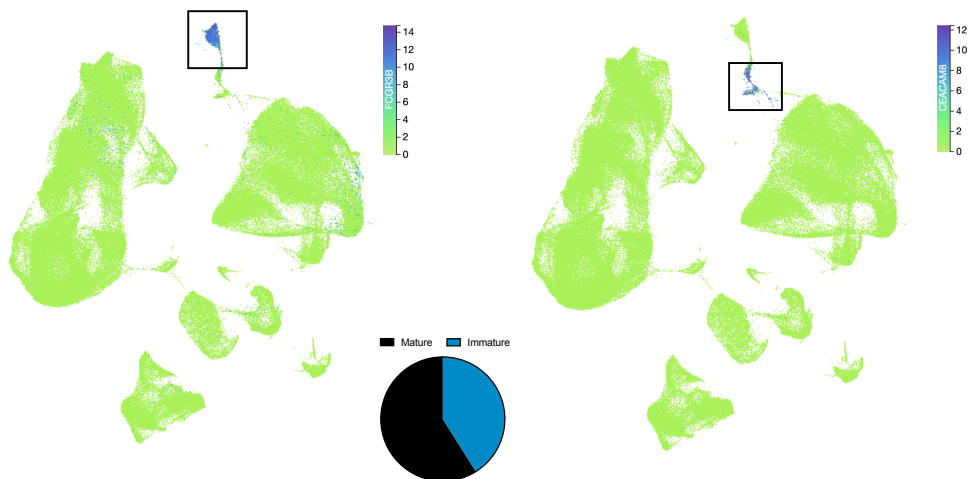
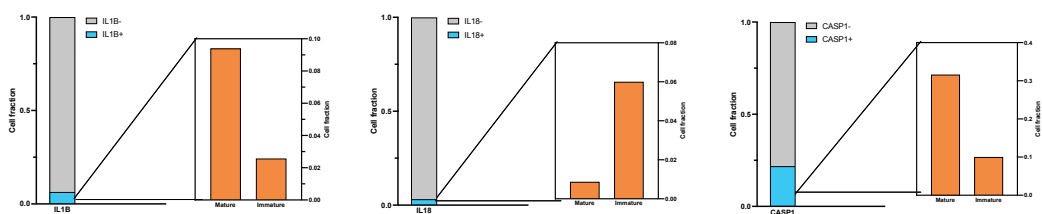
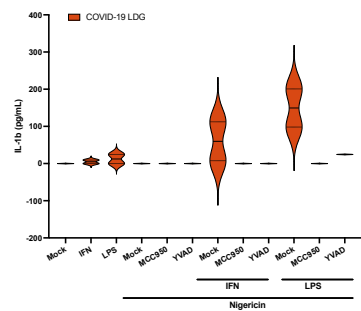
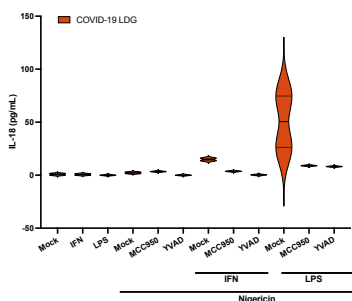
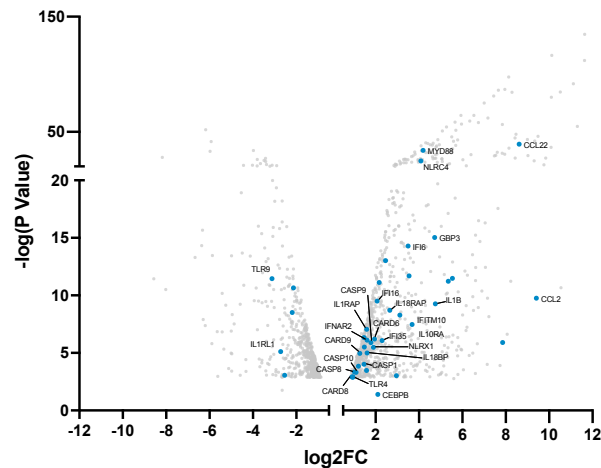
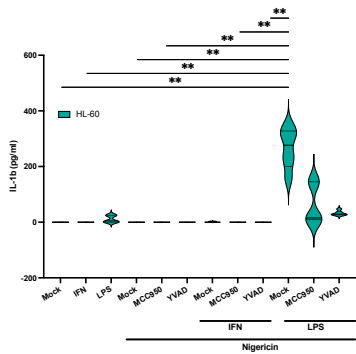
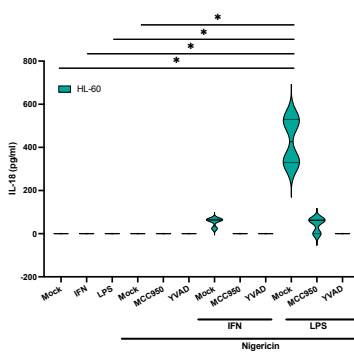


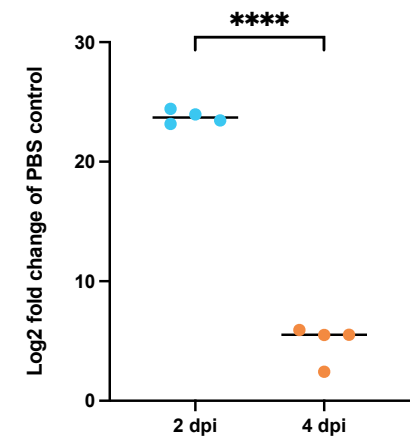
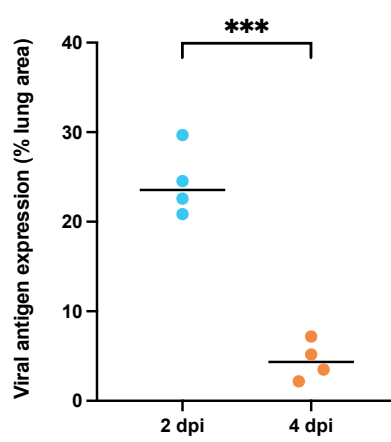
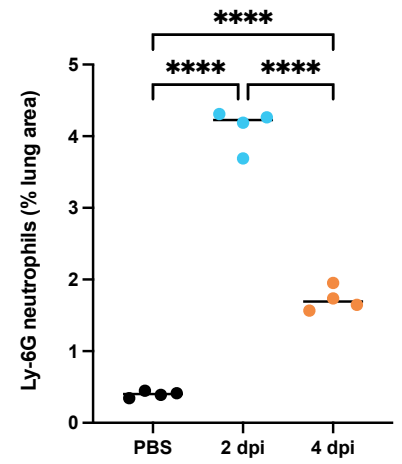
**K**



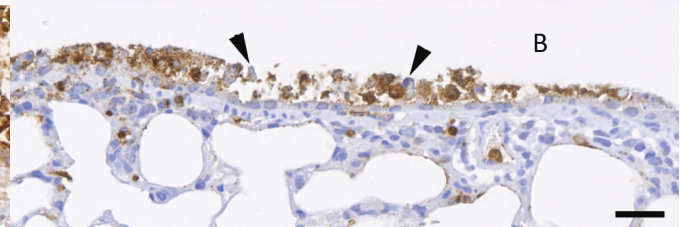
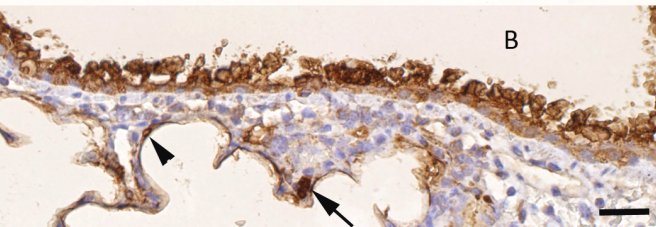
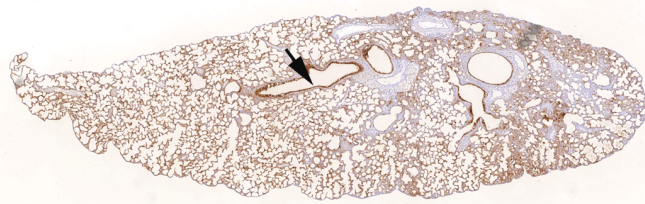
**A****B****C**



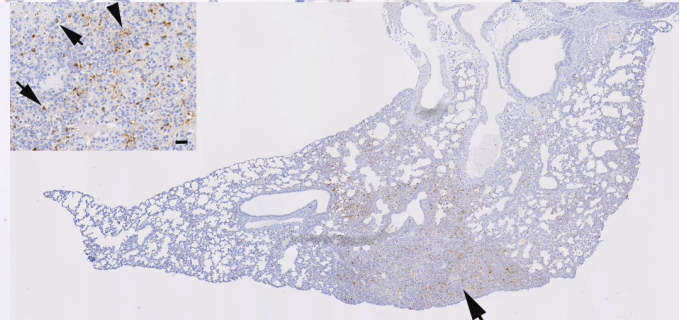
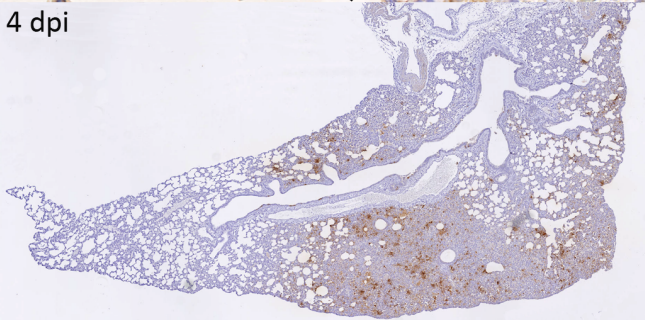
**A****B****C****D****E****H****F****G**

**A****B****C****D****SARS-CoV-2 NP****Ly6G**

2 dpi



4 dpi



Control

